GEOPHYSICS, VOL. 81, NO. 3 (MAY-JUNE 2016); P. D245–D261, 14 FIGS., 3 TABLES.
10.1190/GEO2015-0427.1

A comparative study of the anisotropic dynamic and static elastic moduli of unconventional reservoir shales: Implication for geomechanical investigations

Jaime Meléndez-Martínez[1] and Douglas R. Schmitt[2]

ABSTRACT

We obtained the complete set of dynamic elastic stiffnesses for a suite of "shales" representative of unconventional reservoirs from simultaneously measured P- and S-wave speeds on single prisms specially machined from cores. Static linear compressibilities were concurrently obtained using strain gauges attached to the prism. Regardless of being from static or dynamic measurements, the pressure sensitivity varies strongly with the direction of measurement. Furthermore, the static and dynamic linear compressibilities measured parallel to the bedding are nearly the same whereas those perpendicular to the bedding can differ by as much as 100%. Compliant cracklike porosity, seen in scanning electron microscope images, controls the elastic properties measured perpendicular to the rock's bedding plane and results in highly nonlinear pressure sensitivity. In contrast, those properties measured parallel to the bedding are nearly insensitive to stress. This anisotropy to the pressure dependency of the strains and moduli further complicates the study of the overall anisotropy of such rocks. This horizontal stress insensitivity has implications for the use of advanced sonic logging techniques for stress direction indication. Finally, we tested the validity of the practice of estimating the fracture pressure gradient (i.e., horizontal stress) using our observed elastic engineering moduli and found that ignoring anisotropy would lead to underestimates of the minimum stress by as much as 90%. Although one could ostensibly obtain better values or the minimum stress if the rock anisotropy is included, we would hope that these results will instead discourage this method of estimating horizontal stress in favor of more reliable techniques.

INTRODUCTION

Modern massive hydraulic stimulation programs have allowed low-permeability "tight" and organic-rich rocks, usually generically referred to as "shales" despite their true provenance, to be increasingly considered as exploitable oil and gas reservoirs (Curtis, 2002; Douglas et al., 2011). However, the physical characteristics of such rocks remain poorly known compared to more conventional sands and carbonate reservoir rocks. The mechanical properties of these unconventional reservoir rocks need to be even better understood given the importance in applied seismology to detect "sweet spots" in the reservoir and to more accurately locate microseismic events and in engineering to plan for hydraulic fracture design and to predict stress states (e.g., Iverson, 1995).

Such rocks have long been known to be mechanically anisotropic. The observed anisotropy in shales is intrinsic to the rock itself and is associated with their microstructure, which comprises layering (bedding), preferred mineralogical alignment, and orientations of cracks and pores because of depositional and diagenetic processes. As a result, we usually assume that such rocks will have one axis of rotational symmetry and be transversely isotropic (TI). Despite the importance of shale anisotropy, there are few anisotropy measurements because it is difficult to measure on weak shales and consequently it is usually ignored. Furthermore, most of the existing studies focus solely on comparing measurements made in directions perpendicular and parallel to the specimen's axis of symmetry. Only a subset has attempted to obtain the complete set of elastic constants required to fully characterize the material.

Manuscript received by the Editor 11 August 2015; revised manuscript received 21 January 2016; published online 12 April 2016.
[1]Formerly University of Alberta, Institute for Geophysical Research, Department of Physics, Edmonton, Alberta, Canada; presently Mexican Petroleum Institute, Department of Quantitative Geophysics, Mexico City, Mexico. E-mail: melendez@ualberta.ca; jaimem@imp.mx.
[2]University of Alberta, Institute for Geophysical Research, Department of Physics, Edmonton, Alberta, Canada. E-mail: dschmitt@ualberta.ca.

This contribution begins first with a brief review of the existing literature followed by an overview of theoretical developments that allow us to calculate the stiffnesses, to make a proper comparison between the static and dynamic moduli, and to place these measurements in a context that is more familiar to engineers. To reduce the effects of material heterogeneity, we measure wave speeds through prisms machined from single core pieces that force the waves to all cross within the material. At the same time, we measure static strains on the samples and derive from these linear moduli that allow for direct comparisons to the ultrasonic data. We find that the comparison between static and dynamic values also vary with direction in the material. This issue has become increasingly important in recent years because of the use of sonic log data as a proxy in predicting static geomechanical moduli and strengths. The use of a value of Poisson's ratio derived from such sonic log observations is also popular in predicting horizontal stress magnitudes under a highly restrictive set of assumptions, and we provide additional information here that urges workers to avoid this approach to stress estimation.

We conclude with some thoughts regarding the application of these results to applied seismology and to the use of geophysical observations to engineering practice.

BACKGROUND

Prior work

Ultrasonic wave speed measurements were used to evaluate anisotropy on generic shales by Kaarsberg (1959) who first linked the textures of shales and some carbonates to the preferential alignment of clay minerals. He noted the rotational symmetry of such rocks indicated that they are TI. Hereafter, for the sake of convenience, we will equate this symmetry axis with the vertical. He found significant differences in the P-wave speeds measured at room pressure vertically and horizontally through several artificial samples and on cores taken from western Canada and the USA.

A large number of workers have since continued these studies (see compilations in Thomsen [1986] and Cholach and Schmitt [2006]). As in Kaarsberg's work, anisotropy is determined by comparison of vertical to horizontal wave speeds. These may be sufficient if one assumes elliptical anisotropy as is often done in engineering studies but may be inadequate if more detailed descriptions are required to properly account for obliquely traveling P- and SV-mode waves through the material.

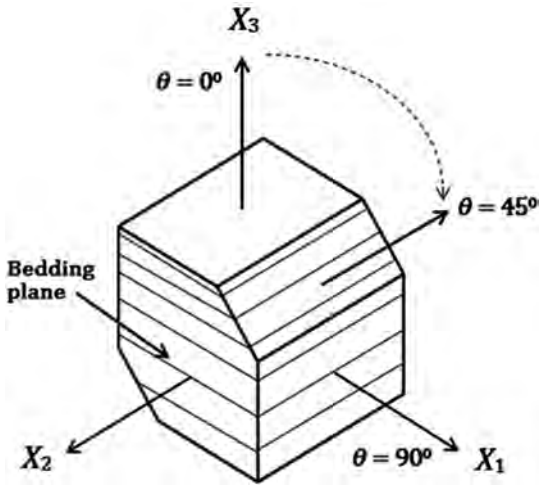

Figure 1. Schematic of the geometry used in the experiment to characterize a TI rock with a presumed axis of rotational symmetry parallel to the x_3-axis. The angle of propagation is measured from x_3 toward the $x_1 - x_2$-plane. The oblique orientation measurements are taken at $\theta = 45°$.

Measuring the complete set of TI elastic stiffnesses demands that wave speeds can also be measured at angles intermediate to the vertical (x_3) and horizontal (x_1 and x_2) axes (Figure 1) (Jones and Wang, 1981; Sondergeld and Rai, 1992; Vernik and Nur, 1992; Johnston and Christensen, 1994; King et al., 1994; Kebaili and Schmitt, 1997; Liao et al., 1997; Horsrud et al., 1998; Hornby, 1998; Jakobsen and Johansen, 2000; Mah and Schmitt, 2001; Wang, 2002; Arroyo and Muir Wood, 2003; Hemsing, 2007; Sarout et al., 2007; Wong et al., 2008; Dewhurst et al., 2011; Blum et al., 2013; Cheng et al., 2013; Meléndez-Martínez and Schmitt, 2013; Sone and Zoback, 2013; Mahmoudian et al., 2014; Sarout et al., 2014; Allan et al., 2015; Xie et al., 2015). Static measurements can be even more cumbersome, and correspondingly, there are fewer such measurements of shale anisotropy (Chenevert and Gatlin, 1965; McLamore and Gray, 1967; Niandou et al., 1997; Gautam and Wong, 2006; Higgins et al., 2008).

Dynamic moduli of anisotropic rocks are important to know because the contribution of their intrinsic anisotropy on the anisotropy observed at seismic scales must be considered when assisting seismic studies such image and depth estimation (Banik, 1984), and amplitude versus offset analysis (Wright, 1987). On the other hand, proxy information on static moduli is necessary for the development of borehole stability and mechanical modeling to avoid drilling-related failures, particularly in areas that show strong anisotropy due to the presence of weak bedding and fractures (Zhang, 2013). Static stress-dependent moduli are also used in hydraulic fracturing modeling to generate a high fracture conductivity path to enhance hydrocarbon production (Meyer and Jacot, 2001).

The adjective "dynamic" is used here to describe those moduli obtained from elastic wave-velocity measurements. In contrast, static moduli are derived directly from the stress-strain relations observed in quasistatic deformational experiments as might be carried out on mechanical testing machines. The dynamic and static moduli should be the same for an ideal elastic material. In reality, they often differ significantly for rocks with the dynamic moduli most commonly greater than the static moduli. Tutuncu et al. (1998) report that, for pressures <20 MPa, dynamic moduli are up to six times higher than static moduli on sandstones, indicating that such dissimilarities can be due to differences in the frequency and the strain amplitude of the two methods (ultrasonic and strain gauges) used during measurements. Simmons and Brace (1965) find that, on granite samples, dynamic moduli were twice the static moduli at 0 MPa and did not become approximately equal until confining pressures of 300 MPa were reached. Similar results were obtained on sandstone, limestone oil shale, and biotite schist samples by Cheng and Johnston (1981) and King (1983). Wong et al. (2008) observe that, at 6 MPa, anisotropic dynamic moduli were up to four times higher than anisotropic static moduli on "wet" shale samples. Behura et al. (2009) measure the dynamic shear wave (SH) anisotropy on Green River oil shales over frequencies from 10 mHz to 80 Hz over the temperature range from 30°C to 350°C on samples that are cut parallel and perpendicular to the bedding. This showed a temperature dependence to the SH anisotropy and attenuation. Holt

et al. (2012) recently find a correlation between static and dynamic moduli in two shales. Sone and Zoback (2013), too, examine this issue in a few shales and find complications with regard to clay contents and whether the comparisons were made on loading or unloading cycles.

There are many reasons for this dispersion between static and dynamic values, and some care needs to be taken when discussing them. One should perhaps think of this more properly as a dispersion of the moduli either with frequency or with time. Regarding the latter, geomechanics engineers are concerned with issues of consolidation in poroelasticity and with the limiting quasistatic "undrained" or "drained" moduli (e.g., Wang, 2000). Undrained moduli describe the deformation produced instantaneously with the application of a stress, and although not often linked, it is exactly the same as that derived by Gassmann (1951) used widely for seismic fluid substitution calculations by geophysicists. The drained modulus is obtained at a sufficiently long time after the material is stressed to allow for any excess fluid to drain out and for pore pressure to reach an equilibrium. If this pore pressure is allowed to completely dissipate to atmospheric, then drained moduli are in principle the same as those measured dynamically on a dry sample.

Alternatively, dispersion of moduli and subsequently wave speeds with frequency is affected strongly by pore fluids. Formally, Gassmann's (1951) formula rigorously provides the moduli at zero frequency. More sophisticated models that account for differential global (e.g., Biot, 1956a, 1956b) or local (e.g., Mavko and Nur, 1975) motions of the pore fluids as mechanical waves pass or phenomenological anelasticity (e.g., Carcione, 2007) must be invoked to account for this.

To obtain the full set of elastic moduli of an ideal vertically transversely isotropic (VTI) medium, velocities with different particle polarization must be measured in a minimum of three different directions: perpendicular, parallel, and oblique to the material's rotational axis of symmetry. Here, to take the velocity measurements, a prismlike-shaped sample is trimmed in different orientations from a main core as shown in Figure 1: perpendicular to bedding (along symmetry axis x_3, $\theta = 0°$), parallel to bedding (within plane $x_1 - x_2$, $\theta = 90°$), and oblique to bedding, i.e., between symmetry axis x_3 and plane $x_1 - x_2$ (usually at $\theta = 45°$). This geometry differs from most comparable studies that measure the anisotropy on core cylinders and has the advantage that the transmitting and receiving piezoelectric transducers always directly face one another across the sample. Furthermore, issues of heterogeneity are reduced as all ultrasonic beams in the different directions all intersect in the prism's center. Static measurements are simultaneously taken along the symmetry axis x_3 and within the $x_1 - x_2$ plane. The measurements are carried out on a suite of different rocks all generically characterized as shales. In addition to a comparison of the dynamic to static moduli, we find that the anisotropy of these rocks is further complicated by pressure dependencies that vary with direction.

Theoretical background

The goal of the current study is to obtain the complete set of elastic constants under the assumption that the material is TI and then to make some comparisons of these to "static" moduli. There exist many discussions of elasticity and anisotropy in the literature (e.g., Auld, 1973), and only a brief introduction is necessary here. We give Hooke's law in reduced Voigt form (Nye, 1985) in which the tensors may be represented by a stress vector $[\sigma_{11} \quad \sigma_{22} \quad \sigma_{33} \quad \sigma_{23} \quad \sigma_{13} \quad \sigma_{12}] = [\sigma_1 \quad \sigma_2 \quad \sigma_3 \quad \sigma_4 \quad \sigma_5 \quad \sigma_6]$ and a strain vector $[\varepsilon_{11} \quad \varepsilon_{22} \quad \varepsilon_{33} \quad \varepsilon_{23} \quad \varepsilon_{13} \quad \varepsilon_{12}] = [\varepsilon_1 \quad \varepsilon_2 \quad \varepsilon_3 \quad \varepsilon_4 \quad \varepsilon_5 \quad \varepsilon_6]$ with a maximum of 21 possible elastic stiffnesses $C_{ij} (= C_{ji})$:

$$\begin{bmatrix} \sigma_{xx} \\ \sigma_{yy} \\ \sigma_{zz} \\ \tau_{yz} \\ \tau_{zx} \\ \tau_{xy} \end{bmatrix} = \begin{bmatrix} C_{11} & C_{12} & C_{13} & C_{14} & C_{15} & C_{16} \\ C_{21} & C_{22} & C_{23} & C_{24} & C_{25} & C_{26} \\ C_{31} & C_{32} & C_{33} & C_{34} & C_{35} & C_{36} \\ C_{41} & C_{42} & C_{43} & C_{44} & C_{45} & C_{46} \\ C_{51} & C_{52} & C_{53} & C_{54} & C_{55} & C_{56} \\ C_{61} & C_{62} & C_{63} & C_{64} & C_{65} & C_{66} \end{bmatrix} \begin{bmatrix} \varepsilon_{xx} \\ \varepsilon_{yy} \\ \varepsilon_{zz} \\ 2\varepsilon_{yz} \\ 2\varepsilon_{zx} \\ 2\varepsilon_{xy} \end{bmatrix}. \tag{1}$$

Conversely, Hooke's law may be written in terms of the compliances S_{ij},

$$\begin{bmatrix} \varepsilon_{xx} \\ \varepsilon_{yy} \\ \varepsilon_{zz} \\ 2\varepsilon_{yz} \\ 2\varepsilon_{zx} \\ 2\varepsilon_{xy} \end{bmatrix} = \begin{bmatrix} S_{11} & S_{12} & S_{13} & S_{14} & S_{15} & S_{16} \\ S_{21} & S_{22} & S_{23} & S_{24} & S_{25} & S_{26} \\ S_{31} & S_{32} & S_{33} & S_{34} & S_{35} & S_{36} \\ S_{41} & S_{42} & S_{43} & S_{44} & S_{45} & S_{46} \\ S_{51} & S_{52} & S_{53} & S_{54} & S_{55} & S_{56} \\ S_{61} & S_{62} & S_{63} & S_{64} & S_{65} & S_{66} \end{bmatrix} \begin{bmatrix} \sigma_{xx} \\ \sigma_{yy} \\ \sigma_{zz} \\ \tau_{yz} \\ \tau_{zx} \\ \tau_{xy} \end{bmatrix}, \tag{2}$$

which is a form that will expedite comparisons of dynamic to static moduli later.

With reference to a VTI solid with the axis of rotational symmetry being vertical and the isotropy plane being horizontal as described in Figure 1, a TI medium is described by only five independent stiffnesses:

$$C_{IJ} = \begin{bmatrix} C_{11} & C_{11} - 2C_{66} & C_{13} & 0 & 0 & 0 \\ C_{11} - 2C_{66} & C_{11} & C_{13} & 0 & 0 & 0 \\ C_{13} & C_{13} & C_{33} & 0 & 0 & 0 \\ 0 & 0 & 0 & C_{44} & 0 & 0 \\ 0 & 0 & 0 & 0 & C_{44} & 0 \\ 0 & 0 & 0 & 0 & 0 & C_{66} \end{bmatrix} \tag{3}$$

or compliances

$$S_{IJ} = \begin{bmatrix} S_{11} & S_{11} - S_{66}/2 & S_{13} & 0 & 0 & 0 \\ S_{11} - S_{66}/2 & S_{11} & S_{13} & 0 & 0 & 0 \\ S_{13} & S_{13} & S_{33} & 0 & 0 & 0 \\ 0 & 0 & 0 & S_{44} & 0 & 0 \\ 0 & 0 & 0 & 0 & S_{44} & 0 \\ 0 & 0 & 0 & 0 & 0 & S_{66} \end{bmatrix}. \tag{4}$$

Note that, in general, $C_{IJ} = S_{IJ}^{-1}$, but the direct expressions relating the stiffness and compliance coefficients directly are also readily available (e.g., Auld, 1973; Lubarda and Chen, 2008; Sayers, 2013).

One purpose of this paper is to link dynamic to static moduli and, as such, it is useful to also provide this result in terms of Young's

moduli E_i, shear moduli G_{ij}, and Poisson's ratios ν_{ij} that are more familiar in engineering and can be related to deformations generated in simple experiments. Geophysicists primarily use the Voigt compliance matrix because of its utility to calculate seismic wave speeds. Conversely, the stresses and deformations are more critical in geomechanical studies. The engineering forms also allow for clear illustration of some interesting aspects of anisotropy, and it also reveals some interesting symmetries with respect to the behavior of stress and strains that is not at all apparent in the forms of equations 3 and 4. Engineers must be concerned with the actual strains that can exist, and examining Hooke's law in this light is useful for making the connections between seismology and engineering.

One can define horizontal (in the $x_1 - x_2$ plane with subscript h) and vertical (in the plane containing x_3-axis with subscript v) Young's moduli $E_h \neq E_v$ and shear moduli $G_{hh} \neq G_{vh} (= G_{hv})$, respectively. One can also define three Poisson's ratios, ν_{hh}, ν_{hv}, and ν_{vh}, that give the lateral Poisson strain induced by imposing a longitudinal strain in the directions indicated by the second and the first subscripts, respectively. For example, ν_{vh} is the Poisson's ratio for the horizontal strain induced when applying a vertical directed uniaxial stress. If so desired, one may also calculate these parameters with respect to a rotated coordinate frame (Li, 1976; Marmier et al., 2010). The Voigt-reduced compliance matrix becomes (see also Lekhnitskii [1981] and Amadei [1983] for more general forms)

$$S_{IJ} = \begin{bmatrix} \frac{1}{E_h} & -\frac{\nu_{hh}}{E_h} & -\frac{\nu_{vh}}{E_v} & 0 & 0 & 0 \\ -\frac{\nu_{hh}}{E_h} & \frac{1}{E_h} & -\frac{\nu_{vh}}{E_v} & 0 & 0 & 0 \\ -\frac{\nu_{hv}}{E_h} & -\frac{\nu_{hv}}{E_h} & \frac{1}{E_v} & 0 & 0 & 0 \\ 0 & 0 & 0 & \frac{1}{G_{vh}} & 0 & 0 \\ 0 & 0 & 0 & 0 & \frac{1}{G_{hv}} & 0 \\ 0 & 0 & 0 & 0 & 0 & \frac{1}{G_{hh}} \end{bmatrix} = \begin{bmatrix} \frac{1}{E_h} & -\frac{\nu_{hh}}{E_h} & -\frac{\nu_{vh}}{E_v} & 0 & 0 & 0 \\ -\frac{\nu_{hh}}{E_h} & \frac{1}{E_h} & -\frac{\nu_{vh}}{E_v} & 0 & 0 & 0 \\ -\frac{\nu_{vh}}{E_v} & -\frac{\nu_{vh}}{E_v} & \frac{1}{E_v} & 0 & 0 & 0 \\ 0 & 0 & 0 & \frac{1}{G_{vh}} & 0 & 0 \\ 0 & 0 & 0 & 0 & \frac{1}{G_{hv}} & 0 \\ 0 & 0 & 0 & 0 & 0 & \frac{2(1+\nu_{hh})}{E_h} \end{bmatrix}, \quad (5)$$

where it becomes evident that due to symmetry, we must also have

$$\frac{\nu_{hv}}{E_h} = \frac{\nu_{vh}}{E_v}, \quad (6)$$

which highlights the fact that $\nu_{hv} \neq \nu_{vh}$ as shown by Love (1892), a result that is not necessarily obvious from equations 1 to 4. Within the isotropic $x_1 - x_2$ horizontal plane,

$$G_{hh} = \frac{E_h}{2(1+\nu_{hh})}. \quad (7)$$

With equations 6 and 7, the total number of independent moduli reduces again to only five in equation 5. Careful examination of equation 5 shows $\nu_{ij} = -S_{ij}/S_{ii}$, an expression that will remain true for any rotation of the coordinate axes (Lethbridge et al., 2010). It is also useful to point out that there are thermodynamic constraints on the values that can be taken for the various moduli because elastic strain energies cannot be negative regardless of the deformation (Lempriere, 1968; Pickering, 1970; Raymond, 1970; Lings, 2001; Rovati, 2003; Ting, 2004; Ting and Chen, 2005), which leads to the following constraints for the TI case here:

1) E_h, E_v, G_{hh}, and $G_{vh} > 0$
2) $-1 \leq \nu_{hh} \leq 1$
3) $(1 - \nu_{hh})E_v/E_h - 2\nu_{vh}^2 \geq 0$ and equivalently $(1 - \nu_{hh})E_h/E_v - 2\nu_{hv}^2 \geq 0$.

The main result is that Poisson's ratios for a TI medium need not fall within the expected range of $-1 \leq \nu \leq$ that we are familiar with for isotropic media (Rovati, 2003) and in some cases can be significantly outside these bounds (Ting and Chen, 2005).

The corresponding stiffnesses in engineering notation are considerably more tedious (Bower, 2010; Nemeth, 2011):

$$C_{IJ} = \begin{bmatrix} \frac{E_h(1-\nu_{vh}\nu_{hv})}{\Delta} & \frac{E_h(\nu_{hh}+\nu_{vh}\nu_{hv})}{\Delta} & \frac{E_h(\nu_{vh}+\nu_{hh}\nu_{vh})}{\Delta} & 0 & 0 & 0 \\ \frac{E_h(\nu_{hh}-\nu_{vh}\nu_{hv})}{\Delta} & \frac{E_h(1-\nu_{vh}\nu_{hv})}{\Delta} & \frac{E_h(\nu_{vh}+\nu_{hh}\nu_{vh})}{\Delta} & 0 & 0 & 0 \\ \frac{E_h(\nu_{vh}+\nu_{hh}\nu_{vh})}{\Delta} & \frac{E_h(\nu_{vh}+\nu_{hh}\nu_{vh})}{\Delta} & \frac{E_v(1-\nu_{hh}^2)}{\Delta} & 0 & 0 & 0 \\ 0 & 0 & 0 & G_{vh} & 0 & 0 \\ 0 & 0 & 0 & 0 & G_{vh} & 0 \\ 0 & 0 & 0 & 0 & 0 & G_{hh} \end{bmatrix} \quad (8a)$$

with

$$\Delta = 1 - \nu_{hh}^2 - 2\nu_{hv}\nu_{vh} - 2\nu_{hh}\nu_{hv}\nu_{vh}. \quad (8b)$$

Conversely, the engineering parameters may be given in terms of the stiffnesses

$$E_h = \frac{C_{11}^2 C_{33} + 2C_{13}^2 C_{12} - 2C_{11}C_{13}^2 - C_{33}C_{12}^2}{C_{11}C_{33} - C_{13}^2}, \quad (9a)$$

$$E_v = \frac{C_{11}^2 C_{33} + 2C_{13}^2 C_{12} - 2C_{11}C_{13}^2 - C_{33}C_{12}^2}{C_{11}^2 - C_{12}^2}, \quad (9b)$$

$$\nu_{hh} = \frac{C_{12}C_{33} - C_{13}^2}{C_{11}C_{33} - C_{13}^2}, \quad (9c)$$

$$\nu_{vh} = \frac{C_{13}C_{11} - C_{12}C_{13}}{C_{11}^2 - C_{12}^2}, \quad (9d)$$

$$\nu_{hv} = \frac{C_{11}C_{13} - C_{12}C_{13}}{C_{11}C_{33} - C_{13}^2}, \quad (9e)$$

$$G_{hh} = C_{66}, \quad (9f)$$

and

$$G_{hv} = C_{44} = C_{55}. \tag{9g}$$

This is somewhat unfortunate because considerable error will propagate through the equations in calculating the Young's moduli and Poisson's ratios using stiffnesses obtained from wave speed measurements.

Relationships between wave speeds and moduli

The TI stiffnesses can be determined from measurements of the wave speeds at strategic directions (Auld, 1973) with

$$C_{11} = \rho V^2_{\mathrm{P}_{90^\circ}}, \tag{10a}$$

$$C_{33} = V^2_{\mathrm{P}_{0^\circ}}, \tag{10b}$$

$$C_{44} = \rho V^2_{\mathrm{S}_{0^\circ}}, \tag{10c}$$

$$C_{66} = \rho V^2_{\mathrm{SH}_{90^\circ}}, \tag{10d}$$

$$C_{13} = \left[\frac{(4\rho V^2_{\mathrm{P}_{45^\circ}} - C_{11} - C_{33} - 2C_{44})^2 - (C_{11} - C_{33})^2}{4}\right]^{\frac{1}{2}} - C_{44}, \tag{10e}$$

where the direction of wave propagation in equations 10a–10e corresponds to the angle θ as shown in Figure 1.

To reduce error, the alternative expression to equation 10e was proposed by Hemsing (2007) to estimate C_{13} by using a combination of $V_{\mathrm{P}}(45°)$ and $V_{\mathrm{SV}}(45°)$:

$$C_{13} = \left[\frac{4\rho^2(V^2_{\mathrm{P}}(45°) - V^2_{SV}(45°))^2 - (C_{11} - C_{33})^2}{4}\right]^{\frac{1}{2}} - C_{44}, \tag{11}$$

which has some advantage in that the uncertainty in determining C_{13} is reduced because there are fewer terms and hence fewer errors to propagate. Equations 10 and 11 allow determination of the elastic constants from recorded waveforms via the measured wave speeds under the restrictions that the material is truly TI and that the x_3-axis is aligned with that for the material's rotational symmetry. We have elected here to convert the wave speeds to moduli directly, but we note that Spikes (2014) extends this by using nonlinear least-squares.

However, before continuing, one important caveat in the application of equations 10 and 11 is that they strictly require phase speeds V. Care must be taken in the definition of the wave speeds in anisotropic media because, unlike isotropic media, corresponding phase V (i.e., plane wave with wavefront W') and group v (i.e., ray with wavefront W) speeds generally differ from one another (Figure 2). Furthermore, their respective angles of propagation θ and Θ lead to transit path lengths L and L'. This may be a serious issue if one inadvertently measures group speeds in the laboratory and then applies these directly to equation 11.

That said, in the principal symmetry directions $\theta = \Theta$ and correspondingly $V = v$, equations 10a–10d are rigorously appropriate. However, this is not the case at oblique angles. This has been overcome by use of transducer arrays to allow for unambiguous determination of phase speeds (e.g., Mah and Schmitt, 2003), by exploiting complementary Rayleigh wave modes (Abell and Pyrak-Nolte, 2013; Abell et al., 2014), by assuming that group speeds are what is being measured and developing appropriate relations usually with a minimization procedure (Every and Sachse, 1990; Cheadle et al., 1991; Jakobsen and Johansen, 2000; Dewhurst and Siggins, 2006; Sarout and Guéguen, 2008a), or, most commonly, by assuming that the sample and transducer geometries are appropriate for the direct determination of phase speed (Vernik and Liu, 1997; Hornby, 1998) with small errors estimated to be less than 1% judged as acceptable. We follow these last workers approach here, but note that proper analysis of this problem will require a full modeling of the beam propagation that must include the geometry of the transmitting and receiving piezoelectrics using beam propagation (Bouzidi and Schmitt, 2006) or Kirchoff-type summation of point sources over the transmitter aperture (e.g., Dellinger and Vernik, 1994). Certainly, the transmitter aperture (15 to 25 mm) greatly exceeds the wavelengths (~1 to 3 mm) and in its "near-field" plane-wave conditions exist; however, the difficulty lies in properly accounting for unavoidable beam spreading effects.

Comparison of dynamic to static measurements

In the measurements to be described, we are able to subject the samples to only hydrostatic pressures and as such are unable to obtain a full set of static moduli. Regardless, it is useful to compare the

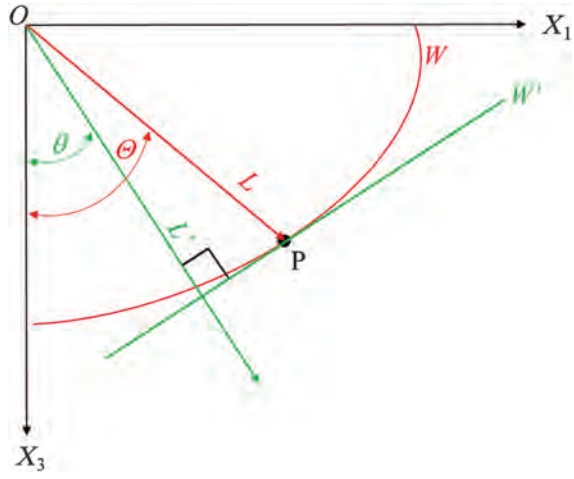

Figure 2. Simplified illustration of the difference between phase and group speeds. Explosive source is activated at time $t = 0$ at the origin O, and rays propagate out in all directions producing at time t wavefront W. An observer at point P will measure a group speed of $v = L/t$ along the ray at group angle Θ. The same observer, however, cannot distinguish the ray arrival from that for the corresponding plane wavefront W' propagating at phase angle θ with speed $V = L'/t$.

observed strains $\varepsilon_0 = \varepsilon_v$ and $\varepsilon_{90} = \varepsilon_h$ with the six wave speeds to make a proper comparison between the static and dynamic measurements. Here, we develop a set of comparative linear moduli that can be determined either from the observed strains or calculated from the dynamic elastic moduli.

A linear compressibility λ_i describes the change in length dL of a fiber of original length L_o parallel to direction i resulting from a change in the applied hydrostatic stress dp (see Brace, 1965),

$$\lambda_i = -\frac{1}{L_o}\frac{dL}{dp} = -\frac{d\varepsilon_i}{dp}. \tag{12}$$

Consequently, the tangent λ_i is simply determined from the derivative of $\varepsilon_i(p)$ observed in the measurements below. Examination of equations 2, 4, and 5 shows, with reference again to the reference frame of Figure 1 under application of the confining pressure p, that $\varepsilon_3 = \varepsilon_v \neq \varepsilon_h = \varepsilon_1 = \varepsilon_2$. Correspondingly, using the stiffness forms equations 1 and 3

$$p = (C_{11} + C_{12})\varepsilon_h + C_{13}\varepsilon_v \tag{13a}$$

and

$$p = 2C_{13}\varepsilon_h + C_{33}\varepsilon_v, \tag{13b}$$

in which solving for ε_v and ε_h and taking the derivative with respect to p gives

$$\lambda_h = \frac{(C_{33} - C_{13})}{(C_{11} + C_{12})C_{33} - 2C_{13}^2} \tag{14a}$$

and

$$\lambda_v = \frac{(C_{11} + C_{12} - 2C_{13})}{(C_{11} + C_{12})C_{33} - 2C_{13}^2}. \tag{14b}$$

Consequently, comparison of the dynamic λ to the static Λ linear compressibilities is, respectively, accomplished by calculating Λ by equation 14 using the stiffnesses derived from the wave speeds measurements and λ by equation 12 from the observed strains, the details of which are described later.

SAMPLE CHARACTERIZATION

Composition and structure

Here, four shale core samples are taken from a cross section of key formations (Table 1) within the Alberta Basin that are of interest for their unconventional resource potential (Rokosh et al., 2012). The trimmed prism-like-shaped samples range 4.12–5.38 cm in height and 5.04–5.99 cm in width. Qualitative assessment of the composition of the samples (Table 2) was obtained using X-ray diffractometry (XRD) for major mineral identification, whole rock X-ray fluorescence (XRF) for chemical proportions and loss on ignition (LOI), and dry combustion after removal of carbonates for total organic carbon (TOC). The structures of the samples were imaged at a variety of scales with thin sections, microscopic X-ray tomography (m-CT), and scanning electron microscopy (SEM).

Some of these cores were cut as early as 1957, and in such cases, desiccation is a potential concern. We do not believe this to be a serious problem for these rocks because they do not appear to contain significant amounts of swelling clays and the cores remain competent. Their porosities are all quite small, and the samples likely never contained large amounts of free pore fluids. Regardless, it is likely that the mobile volatile hydrocarbons that originally resided in the pore spaces are no longer present.

Sample SSA-24 (Figure 3a) is an indurated black shale from the Lower Jurassic Fernie Formation shales according to the associated well logs. This is known to be an important source rock, but it is also currently being examined for its potential as an economic unconventional reservoir (Meyer, 2012). Understanding the anisotropy of this formation is of particular importance for seismic migration as much of this reservoir lies within the tilted sequences of the disturbed belt fronting the Rocky Mountains in Alberta. This sample has particularly simple mineralogy and a high TOC, and the high LOI reflects this as well as loss of OH from the abundant kaolinite. The LOI is used to estimate carbonate and organic content in those sediments (e.g., Dean, 2007).

Macroscopic layering of this sample is not immediately apparent (Figure 3a) but the layering is obvious in the microscopic observations. The thin sections show alternating dark and presumably organic-enriched layers with whiter quartz-rich layers (Figure 4a). In the m-CT images, this layering is also detected as horizontal variations in density, but a series of bedding-parallel cracks (Figure 3b) are also seen, but it is not known if these are related to core damage or produced during hydrocarbon generation (Vernik and Liu, 1997; Kalani et al., 2015). At modest magnification (Figure 4c), SEM shows a clear separation of the organic and mineral content of this rock with much, but not all, of the organic material stretched into bedding-parallel lenticular masses. At even higher magnifications (Figure 4d), this separation of organic and mineral material remains. The organic material displays conchoidal, glasslike fracturing, and appears nonporous at least up to 10,000 times magnification; this contrasts with the porous organic material seen for example by Sondergeld et al. (2010) in a Barnett shale. Cracklike and bedding-parallel porosity is apparent between the clay mineral grains.

Table 1. Depth, location, and geologic formation of shale samples studied.

Sample	Sample depth (m)	Alberta Township system designation	Formation	Lithology
SSA-24	4236.0	16-05-06-01 W5	Fernie	Black Shale
SSA-27	1041.3	10-34-42-22 W4	Second White Speckled Shale	Calcareous mudstone
SSA-41	627.28	11-12-06-16 W4	Second White Speckled Shale	Calcareous mudstone
SSA-42	1647.4	04-08-13-27 W5	Colorado	Calcareous mudstone

Samples SSA-27 (Figure 3b) and SSA-41 are taken from the Upper Cretaceous Second White Speckled Shale (Leckie et al., 1994), a member of the Colorado Group. This member is described as a laminated calcareous mudstone with "white specks" that are cocolithic fecal pellets. This member has long been known to be a prolific source rock but which has also garnered interest as a reservoir on its own (Bloch et al., 1999; Furmann et al., 2015). These two samples contain a more diverse mix of clay minerals (see also extensive compilations in Pawlowicz et al., 2008).

The structures of these samples are broadly similar displaying laminations at a variety of scales. Organic-rich layers (dark) are interleaved with cleaner zones at the millimeter scale (Figure 5a). The texture appears unorganized at 500 times magnification in the SEM (Figure 5b) but more order with preferential alignment of the clay minerals is seen at greater magnifications (Figure 5c). Again, bedding-parallel cracklike pore space is seen between the mineral grains that are primarily micalike illite here. There is less organic material, in agreement with the LOI and TOC measurements, and in contrast to SSA-24, the organic matter it has does not appear to have any texture.

Sample SSA-42 (Figure 3c) is from a rare Upper Colorado Group core also fortuitously studied in detail by Nielsen et al. (2003); based on their log interpretation and on this samples composition, we believe this to come from the bottom of the First White Speckled Shale member of the Niobrara Formation. They refer to this as a calcareous, dark gray shale. This material has the lowest LOI and TOC and has more detrital mineral grains. It too displays layered structure at the millimeter scale (Figure 6a), but under greater magnifications, the detrital grains appear to disrupt any organization of the clay minerals (Figure 6b).

Petrophysical characteristics

A suite of conventional petrophysical measurements (Table 3) including bulk density ρ, grain (solid) density ρ_s, and porosity ϕ were made in our laboratory using He pycnometry (Micromeritics MVP-6DC), envelope volume determinations (Micromeritics Geopyc, 1360), and Hg-injection porosimetry (Micromeritics Autopore IV penetrometer).

The porosities given are all quite low, and there are differences between the two methods used. Both techniques rely on intrusion of either He or Hg into an evacuated sample, and the variations likely reflect the difficulties for the fluids to penetrate the material. These variations further pass to the determination of the bulk density with determination of the envelope volume on a larger sample being subject to substantial uncertainty. As such, in later calculations, we take the Hg-provided measure of ρ.

However, the Hg-injection can also provide additional semiquantitative insight into the material structure. Briefly, the Hg porosimeter works by forcing Hg, a nonwetting liquid, into the pore space of a porous rock by pressure P. The greater the P, the smaller the orifice that the Hg enters; and consequently, if the volume of Hg injected is carefully monitored with increasing P, then one may gain not only an idea of the material porosity but also some indications of the proportions of the pore space accessible by different sized pore orifices. The diameter d of the pore orifice that can be entered is

$$d = -4\lambda \cos(\theta/P), \tag{15a}$$

where λ and θ are the surface tension and wetting angle, respectively. As Hg is nonwetting, substantial pressure is required to force it into the pore space; the instrument used in principle will push Hg into pore orifices as small as 3.5 nm. Further details may be found in Giesche (2006). This technique generally shows that the pore space dimensions are typically small and predominantly range from 4 to 12 nm (Table 3).

Examination of the Hg imbibition and drainage (also called withdrawal) upon initial pressurization followed by depressurization can provide qualitative indications of structure of the pore network

Table 2. Compositional characteristics.

	Mineral Identification (XRD)								Whole Rock Analysis (XRF)[3] Wt%						Dry Combustion[4]		
Sample	Quartz	Kaolinite	Ill/Mus	Doloimite	Calcite	Albite	Pytire	Chlorite	SiO_2	$Al2O_3$	$Fe2O_3$	CaO + MgO	Other	Loss on Ignition	Total N Wt%	TOC wt%	Kerogen[5] Vol%
SSA-24									57.6	17.6	0.8	0.6	3.1	20.1	0.3	13.9	29.9
SSA-27									63.3	9.8	3.1	7.0	10.5	11.9	0.2	3.2	7.4
SSA-41									66.0	9.3	4.1	4.4	7.9	11.3	0.2	4.0	9.0
SSA-42									66.5	10.9	3.6	5.3	8.8	7.2	0.1	1.4	3.5

3. Other oxides include TiO_2, P_2O_5, Cr_2O_3, and V_2O_5.
4. See Charles and Simmons (1986), 6% HCl used to remove carbonates.
5. Volumetric kerogen content estimated from TOC according to Vernik and Nur (1992)

(Wardlaw and McKellar, 1981). Such curves (Figure 7) for the two end-member samples SSA-24 and SSA-42 broadly behave similarly with little Hg entering the sample until pore dimensions of approximately 10 μm are attained but with the bulk entering at much smaller pore sizes. The drainage portions of the curves show that in both cases the major portion of the Hg does not drain out. That is, this Hg is trapped within the complex pore network for numerous reasons (Kloubek, 1981). Indeed, nearly no Hg is returned from SSA-24. These observations are consistent with the low values of the measured ϕ as well as with the microscopic images in Figures 4–6.

METHOD

Experimental procedure

To determine the elastic properties, one must be able to measure wave speeds in a variety of directions through the material. Various workers have done this with several strategies ranging from machin-

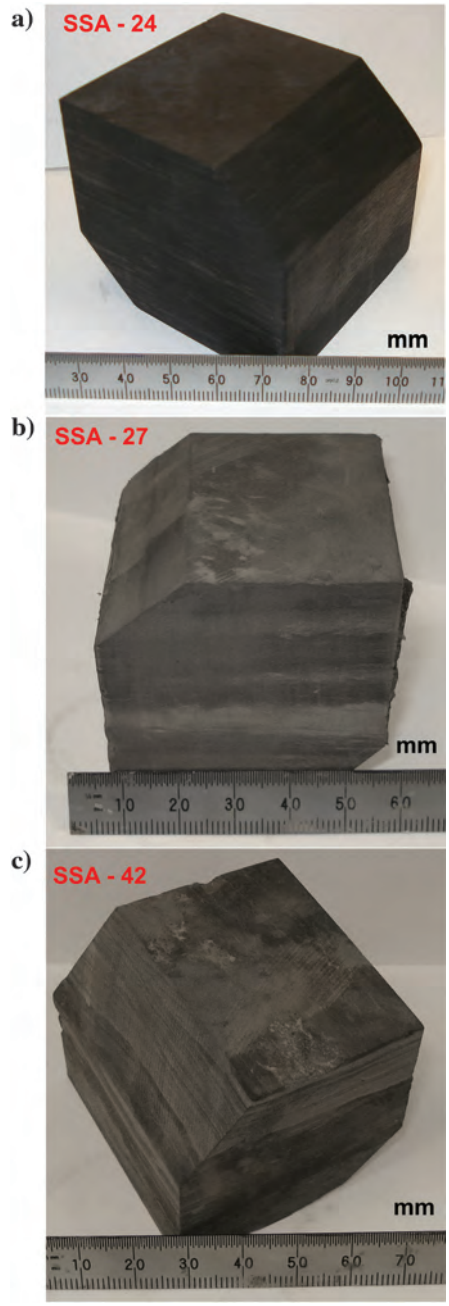

Figure 3. Photographs of shales studied. (a) Fernie Formation sample SSA-24. (b) Lower Colorado Group Second White Speckled Shale Formation sample SSA-27. (c) Upper Colorado Group First White Speckled Shale Member sample SSA-42.

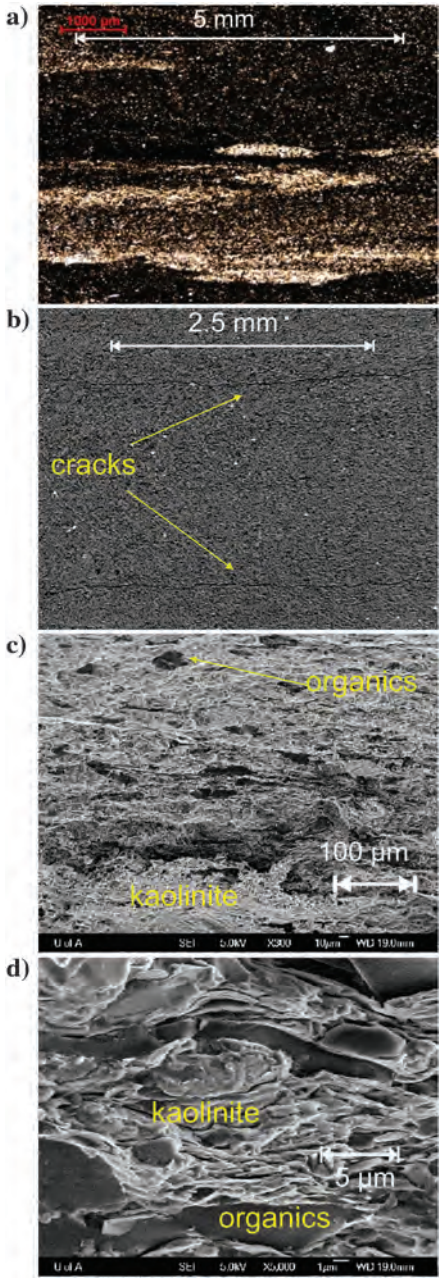

Figure 4. Microscopy on Fernie Formation sample SSA-24. (a) Transmitted light thin section, (b) vertical section through 3D m-CT volume, and (c) SEM image at 300 × s magnification. Organic material is dark and clays bright. (d) SEM images at 2500 × s magnification. This image from highlighted white zone in panel (c).

ing spheres (Lokajicek and Svitek, 2015), multifaced polyhedra (Cheadle et al., 1991; Nara et al., 2011), cylindrical rock specimens (Nadri et al., 2012), or transducer arrays (Kebaili and Schmitt, 1997). Here, dynamic and static measurements were taken on machined prisms with a pressurization cycle of hydrostatic compression to 60 MPa and back. Oil was used as a confining medium. This work extends the technique presented by Wong et al. (2008) and Chan and Schmitt (2015). Dynamic ultrasonic pulse transmission and static strain measurements were made simultaneously on specially machined eight-faced prisms of the core samples (Figure 1). Faces were machined parallel, perpendicular, and at 45° to the bedding plane (Figure 1). The Colorado Group shales were weak and required particular care to obtain a proper test piece. Opposite surfaces were made flat and parallel using a surface grinder. No fluids were used during cutting or flattening to avoid damaging the material.

Copper sheeting was directly epoxied to sections of these surfaces to provide a conductive base for mounting of the ultrasonic components. Longitudinal-mode (1 MHz, 2.54 cm diameter) and transverse-mode (1 MHz, 1.90 cm square)-lead zirconate titanate piezoelectric ceramics were attached to the copper sheeting using conductive silver epoxy. A dedicated signal wire was then also secured to the top of each ceramic. The longitudinal-poled ceramics expand upon activation to primarily create the P and qP modes. The transverse-poled ceramics shear upon activation creating a highly polarized S and qS modes; care must be taken to ensure that a sending-receiving pair of these is correctly oriented with respect to each other. The six pairs of ceramics (Figure 8a) were organized on the sample to most efficiently, but with some redundancy, allow for determination of the five independent C_{ij} according to equations 10. It must be noted that for sample SSA-24, the SH shear mode was obtained at the oblique 45° direction whereas the SV mode was obtained in this direction for all of the remaining samples. As in Wong et al. (2008), no mechanical damping was applied to the ceramics to admit the strongest pulse possible through these lossy materials.

The transmitting ceramics were activated with a fast rising edge 200 V step pulse using a pulser/receiver (JSR-PR35). The signals from receiving transducers were digitized with a sampling period of 10 ns for 10 μs and stored. A full suite of six waveforms was acquired at increments of approximately 3 MPa up to the maximum pressures of 60 MPa and back to room pressure.

The ceramics were directly attached above the copper sheet and as such could not be calibrated as is the normal case when they are mounted on buffer rods. This is a problem because our experience has shown (Molyneux and Schmitt, 2000) that the most physically meaningful and consistent pulse transit times are obtained by picking the first amplitude extremum from which the corresponding transducer calibration time is subtracted. To overcome this difficulty, we carried out calibrations of a subset of the ceramics using a suite of aluminum cylinders of varied length. Analyses of the observed transit times yielded delays of $\Delta t_P = 0.485$ μs and $\Delta t_S = 1.130$ μs for the longitudinal and transverse ceramics, respectively, which correspond to the finite rise time of the ceramics once they have been activated, i.e., the pulser-transducer excitation delay. For further details about ceramic calibrations, see Meléndez-Martínez (2014).

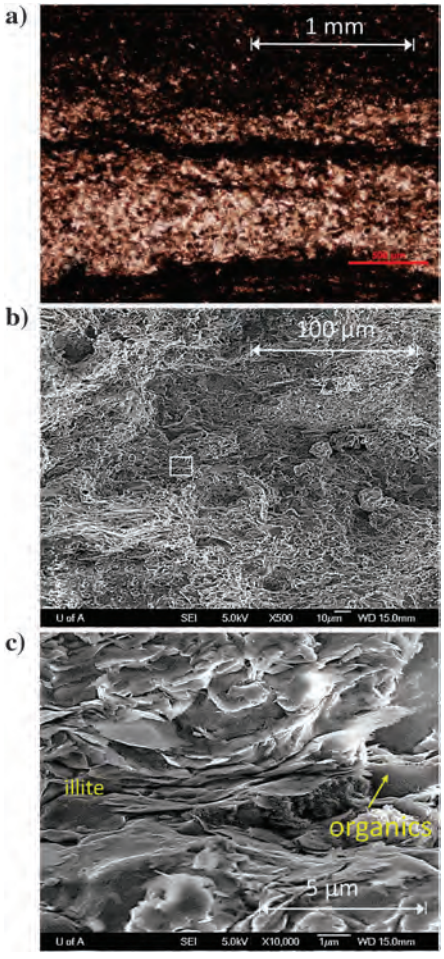

Figure 5. Microscopy from Second White Speckled Shale SSA-27. (a) Transmitted light thin section, (b) SEM image at 500 × s magnification, and (c) SEM images at 10,000 × s magnification. This image from highlighted white zone in panel (b).

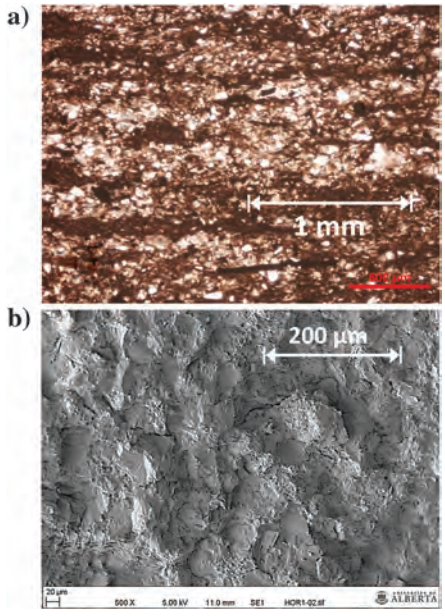

Figure 6. Microscopy from First White Speckled Shale SSA-42. (a) Transmitted light thin section and (b) SEM image at 500 × s magnification.

The sources of uncertainty include the error in measuring the transit path lengths (100 μm) and their contraction under pressure, and time picking including the observed and the delay correction (0.02 μs). We estimate the uncertainties to be 0.3% and 0.2% for P- and S-wave speeds, respectively.

Foil strain gauges (Vishay Micro-Measurements, CEA-06-250UT-350, 350 Ω, gage factor of 2.11) were glued directly on the shale surfaces oriented so as to measure the strains parallel (ε_{90}) and perpendicular (ε_0) to the bedding planes (Figure 8a). The sample is then sealed with urethane putty to avoid leakage of the confining pressure fluid into the sample.

Several authors (Brace, 1964; Milligan, 1967; Kular, 1972) have shown that foil strain gage measurements are affected by confining pressure. To overcome this, following Bakhorji (2010), a fused quartz calibration standard was prepared using the same batch of strain gauges. The standard accompanied the sample into the pressure vessel, and the deviation between its measured strains and those expected using its well-known elastic response (Ohno et al., 2000) yielded pressure-dependent corrections that were applied to the observed sample strain; additional details may be found in Meléndez-Martínez (2014).

Each strain gage in the pressure vessel attached to the sample and the standard completed the fourth arm of its own independent Wheatstone bridge activated by a constant potential of V_{in} = 2.5 volts. The bridges were operated in an "unbalanced" mode in which successive potentials across the bridge V_u and V_s responding to unstrained and strained states, respectively, are measured to determine the strain according to

$$\epsilon = \frac{-4V_r}{G_f(1+2V_r)}, \tag{15b}$$

where

$$V_r = \frac{V_s - V_u}{V_{in}}. \tag{15c}$$

Table 3. Petrophysical characteristics.

Sample	Bulk density ρ (g/cm^3)		Grain density (g/cm^3)		Porosity (%)		Pore throat (nm)
	Envelope	Hg	He	Hg	He	Hg	Hg
SSA-24	2.27	2.34	2.306	2.410	1.5	3.0	6
SSA-27	2.48	2.40	2.490	2.505	<1.0	4.4	11
SSA-41	2.39	2.41	2.462	2.522	3.0	4.3	4–5
SSA-42	2.66	2.60	2.698	2.645	1.6	1.7	6–12

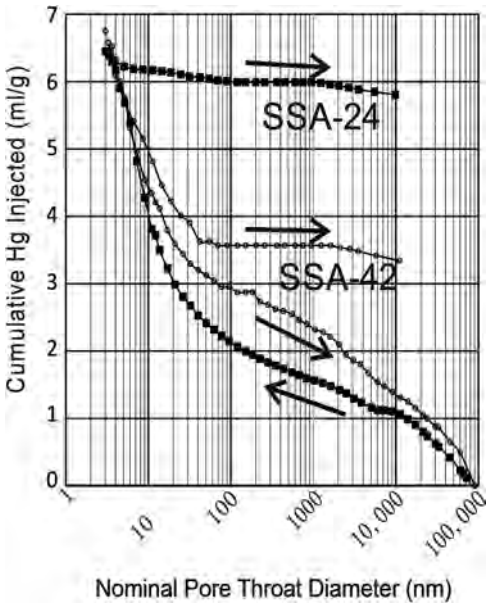

Figure 7. Cumulate Hg imbibed (on pressurization indicted by left pointing arrows) and drained (on depressurization indicated by right-pointing arrows) versus pore orifice diameter d for Fernie Formation SSA-24 (filled squares) and First White Speckled Shale SSA-42 (open circles). Note the inverse relation between pressure and d in equation 15.

RESULTS

Observed wave speeds and Thomsen parameters

As mentioned above, one P-wave and one S-wave traveltime were measured on the directions perpendicular, parallel, and oblique to the bedding for each specimen. Figure 9 shows some examples of the recorded waveforms as a function of confining pressure.

The wave speeds determined for the Fernie Formation (SSA-24) and Colorado Formation, Second White Speckled Shale (SSA-27), and Colorado Formation First White Speckled Shale (SSA-42) are plotted in a directly comparable fashion in Figure 10a–10c, and the corresponding values are provided in the associated electronic supplement as are those for the SSA-41, which is also from the Second White Speckled Shale and which are quite similar to that for SSA-27. One immediate observation is that the wave speeds between the three shales are quite different and likely inversely dependent on the proportion of organic carbon in the sample. Thus, according to Table 2, the lowest TOC weight percentage corresponds to sample SSA-42 that shows the highest waves speeds whereas, conversely, the lowest wave speeds correspond to sample SSA-24 that contains the highest TOC weight percentage. All of the observations are broadly consistent with the assumed transverse isotropy for the samples with $V_P(0°) < V_P(45°) < V_P(90°)$ and $V_S(0°) < V_{SH}(45°) < V_{SH}(90°)$ for sample SSA-24, and $V_S(0°) < V_{SV}(45°) < V_{SH}(90°)$ for samples SSA-27, SSA-41, and SSA-42. Hysteresis effects are observed in all samples; i.e., pressurization velocities are slightly lower than depressurization velocities because of differences in the closing/opening rate of microcracks and pores during the compression/decompression cycles (Gardner et al., 1965).

The degree of anisotropy is provided here in terms of Thomsen's (1986) P-wave $\varepsilon = [V_P(90°) - V_P(0°)]/V_P(0°)$ and SH-wave $\gamma = [V_{SH}(90°) - V_S(0°)]/V_S(0°)$ (Figure 10d–10f). Thomsen (1986) also defines a δ that characterizes off-axis curvature of the qP and qSV modes as

$$\delta = \frac{(C_{13} + C_{44})^2 - (C_{33} - C_{44})^2}{2C_{33}(C_{33} - C_{44})}, \qquad (16a)$$

where we recast here only in terms of the wave speeds that is given as

$$\delta = \frac{[V_P^2(45°) - V_{SV}^2(45°)]^2 - \frac{1}{4}[V_P^2(90°) - V_P^2(0°)]^2 - [V_P^2(0°) - V_{SH}^2(0°)]^2}{2V_P^2(0°)[V_P^2(0°) - V_{SH}^2(0°)]}. \qquad (16b)$$

Both ε and γ respectively, indicate relatively high values in excess of 15% of P- and SH-wave anisotropy for the Fernie (SSA-24) and Second White Speckled (SSA-27) shales at the highest confining pressures. In contrast, these are only approximately 6% for the First White Speckled Shale (SSA-42); this is in qualitative agreement with the textures seen at the thin section and SEM scales where detrital grains break any preferred alignment of the clay minerals and consequently reduce anisotropy. Interestingly, $\varepsilon \sim \delta$ at high confining pressure (> 45 MPa) for this sample suggesting that its anisotropy is nearly elliptical at such pressures.

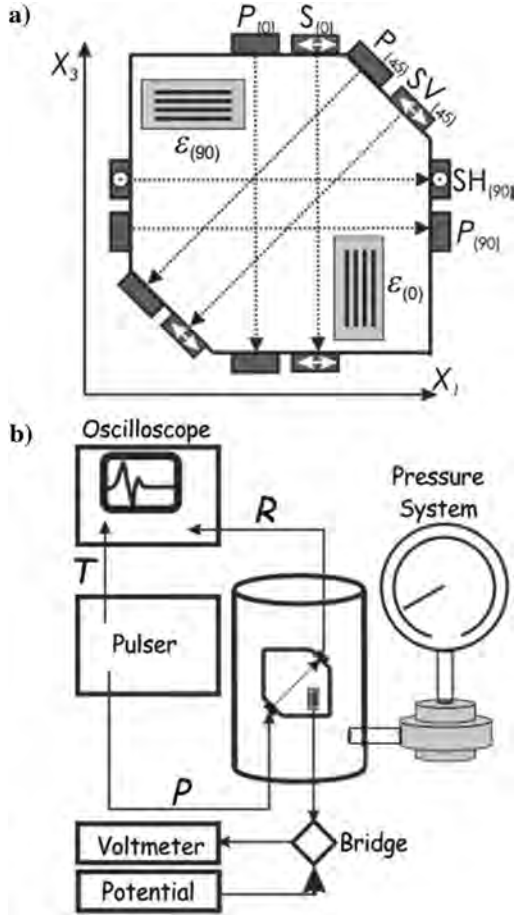

Figure 8. Experimental configuration. (a) Placement and orientations of piezoelectric ceramics and strain gauges. Note that only for sample SSA-24, SV(45) is replaced by SH(45). (b) Simplified experimental set up T, P, and R indicate trigger, active pulse, and received pulse, respectively. Fused quartz strain standard is not shown.

On the other hand, δ shows a change of sign, from positive to negative, for SSA-24 with increasing confining pressure, which could indicate a variation in the elastic properties of the contact areas between clay minerals as pointed out by Sayers (2004) whereas the $\delta > 0.25$ for the Second White Speckled (SSA-27) indicates complexity in its wave surfaces.

The wave speeds all increase with pressure as expected due to the progressive closure of cracklike porosity. However, how the wave speeds evolve with pressure can depend strongly on the direction they are measured. In the Fernie Shale (SSA-24), bedding parallels $V_P(90°)$ and $V_S(90°)$ remain nearly constant over the entire range of confining pressures whereas the changes in the bedding perpendic-

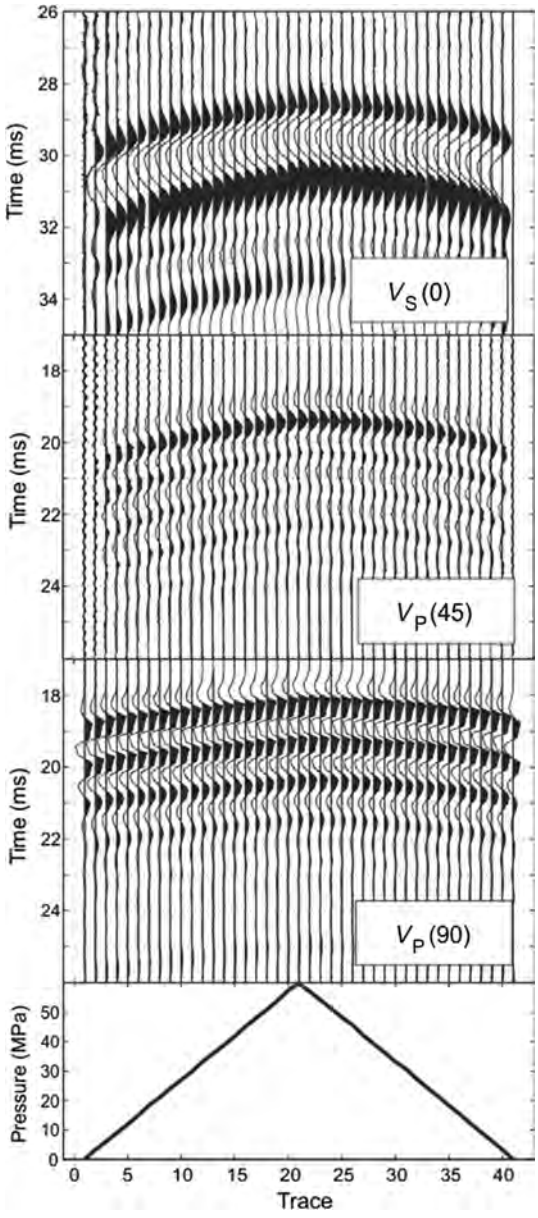

Figure 9. Examples of observed sets of waveforms for the Colorado Formation Second White Speckled Shale (SSA-27) sample. A dependence on traveltime as a function of confining pressure is observed. Lowest panel indicates the confining pressure at which each corresponding trace was obtained.

ulars $V_P(0°)$ and $V_S(0°)$ are substantial and increase nonlinearly. Similar, but muted, behavior is seen for the Second White Speckled Shale (SSA-27), and for this sample, $V_S(0°)$ increases in a linear fashion. All of the wave speeds for the least anisotropic First White Speckled Shale (SSA-42) increase nonlinearly with pressure. These observations are in qualitative agreement with the textures seen in the SEM micrographs. Samples SSA-24 and SSA-27 display bedding-parallel cracklike porosity that is expected to result in the nonlinear behavior of the wave speeds measured perpendicular to bedding. However, to reiterate, the interesting point here is that there is a little variation in the bedding-parallel wave speeds with pressure.

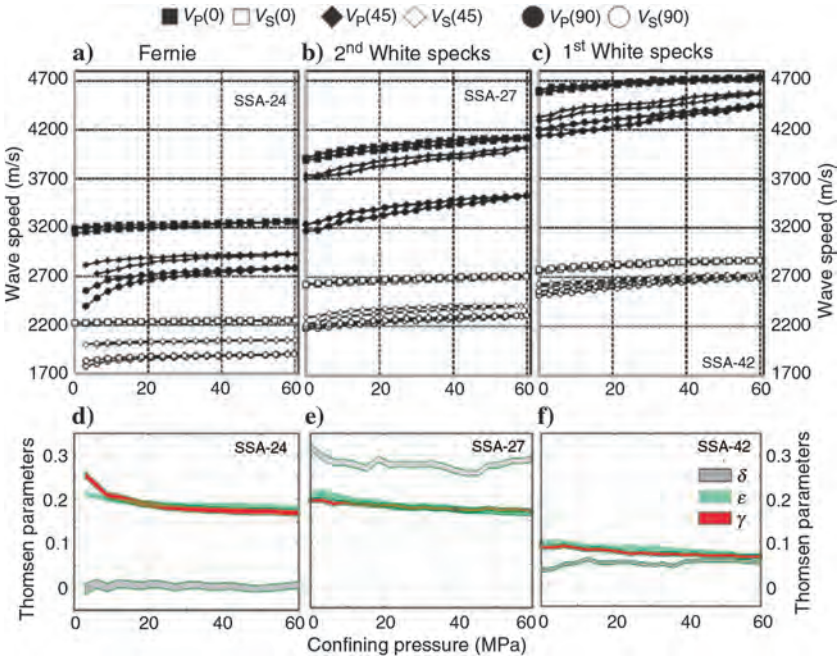

Figure 10. Observed wave speeds with hydrostatic confining pressure for samples (a) SSA-24 Fernie Formation, (b) SSA-27 Second White Specks Formation, and (c) First White Speck Formation. Filled and open symbols represent V_P and V_S, respectively. The shapes of the symbols indicate propagation direction according to squares −0°, diamonds −45°, and circles −90°. The polarizations are illustrated in Figure 8a except for sample SSA-24. Symbols are larger than the expected uncertainty. Derived Thomsen parameters for (d) SSA-24 Fernie Formation, (e) SSA-27 Second White Specks Formation, and (f) First White Speck Formation. Gray, green, and red lines represent the Thomsen (1986) parameters, δ, ε, and γ, respectively, with the line widths equal to the uncertainty envelope computed by statistical propagation of error.

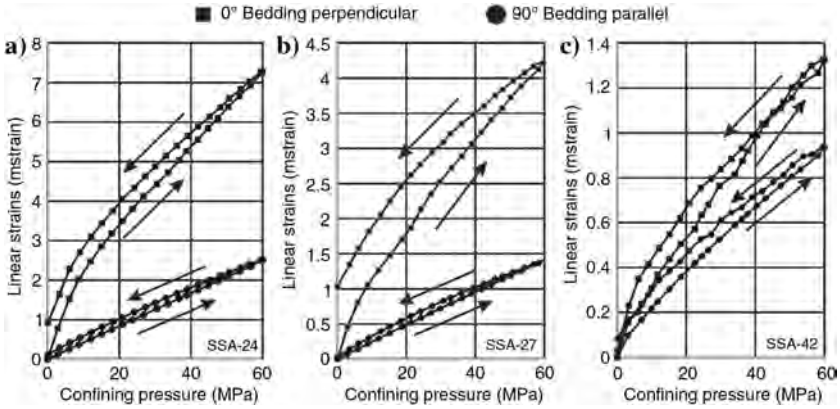

Figure 11. Pressure-corrected strains in the horizontal (90° bedding parallel — filled circles) and vertical (0° bedding perpendicular — filled squares) strains observed during pressurization-depressurization cycle as indicated by upward and downward going arrows, respectively, for (a) Fernie Formation sample SSA-24, (b) Second White Specks Formation sample SSA-27, and (c) First White Specks Formation sample SSA-42.

Observed strains

The pressure-corrected strains ε_{90} and ε_0 also display directional behavior (Figure 11) It is important to note the variations in the scales for the strain between the three samples. Sample SSA-42 is particularly stiff such that the strains are significantly smaller than for the other samples, and as such, the relative noise is greater. The bedding-parallel ε_{90} varies nearly linearly with the confining pressure, P_c, contrasting with the nonlinear behavior of the bedding-perpendicular ε_0. Furthermore, $\varepsilon_{90} < \varepsilon_0$ in all cases, indicating that these rocks are all more compressible perpendicular to bedding than parallel to bedding, and this is entirely consistent with the pressure dependencies for the ultrasonic wave speeds described above.

DISCUSSION

Dynamic moduli

The dynamic moduli (Figure 12a–12c), calculated from the observed wave speeds using equations 10, further highlight the variations in the anisotropy in these samples. As a simple check on reliability, the moduli satisfy all of the inequalities demanded by thermodynamics. Failure to pass these tests that allow for quite broad variations in moduli would indicate either that the measurements were erroneous or that the underlying assumptions used in the current analysis were not valid. Figure 12 also includes the Young's moduli and Poisson's ratios calculated from equations 9. As already seen, all of these rocks are more compressible perpendicular to bedding that parallel to bedding and subsequently $C_{11} > C_{33}$, $E_h > E_v$ and $C_{66}(= G_{hh}) > C_{44}(= G_{hv} = G_{vh})$. Aside from some of the results at low pressure for sample SSA-24, generally $\nu_{hh} < \nu_{vh} < \nu_{hv}$, which again reflects the greater stiffness of the horizontal $x_1 - x_2$ plane within these materials. According to Sayers' (2013) modeling, the observation that $\nu_{hv}/\nu_{hh} > 1$ is what would be expected in a shale with some preferential alignment of the clay minerals.

The three samples display quite different behaviors in terms of the relative values of the differing moduli. The high TOC sample SSA-24 is by far the most anisotropic, but it is of particular interest in that it has off-axis values of $C_{13} \approx C_{12}$ that are only a small fraction of the others. This

translates to very small Poisson's ratios less than 0.07 and forces $E_h \approx C_{11}$ and $E_v \approx C_{33}$. This contrasts significantly with SSA-27 with proportionally larger C_{12} and C_{13} leading to a large $\nu_{hv}(\sim 0.35)$ and a small $\nu_{hh}(\sim 0.06)$. The diminished anisotropy in sample SSA-42 is evident as the moduli approach one another.

Static moduli

As already noted, linear strains were measured in two directions because the sample was hydrostatically pressurized, and this allows for determination of only the linear compressibility Λ by simply taking $d\varepsilon/dp$ on the observed strains (Figure 11). For this, we find the tangent to the $\varepsilon - p$ curves that is simple in concept but requires care in application due to unavoidable noise. The most direct approach is to simply calculate the simple differences between subsequent data points with $\Lambda = (\varepsilon_{i+1} - \varepsilon_i)/(p_{i+1} - p_i)$ to provide an estimate of the local slope. This calculation is illustrated by "*" symbols in Figure 13, and it provides reasonable, but noisy, measures. A smoother estimate for Λ was obtained by a parametric fit using

$$\varepsilon(p) = a + bp + cp^{1/2} \tag{17a}$$

from which the derivative is simply taken to obtain the static linear compressibility Λ that is given as

$$\Lambda(p) = \frac{d\varepsilon(p)}{dp} = b + \frac{c}{2}p^{-1/2} \tag{17b}$$

and is shown as lines in Figure 13. The simple equation 17a fits the observed strain curves with correlation coefficients in excess of 0.999, and the resulting tangent moduli track well the more crudely calculated local slope values. Equation 17a is no more than a simple fitting curve. We note that including exponential terms to describe pressure-dependent behavior has long been popular in the rock physics literature (see Schmitt [2015] for a review), but such curves were not able to describe the nonlinear behavior at low confining pressures to our satisfaction leading us to adopt equation 17a instead.

The observed static compressibilities Λ all decrease rapidly with confining pressure, and they further demonstrate the anisotropy of the samples with $\Lambda_v > \Lambda_h$ in all cases. As with the other moduli, Λ_h is significantly less pressure sensitive than Λ_v. Therefore, the behavior of the static moduli tracks that for the dynamic moduli.

The dynamic linear compressibilities λ, as calculated using the elastic stiffnesses according to equation 14, are shown as open circles in Figure 13. This allows for direct comparison of static and dynamic moduli, and an interesting pattern emerges with $\Lambda_v > \lambda_v$ in all cases but significantly so for SSA-24 and SSA-27 being near 100% larger even at the highest confining pressure; $\Lambda_h > \lambda_h$ also in all cases, but in contrast to the vertical compressibilities, this difference is small. Indeed, at pressures greater than 30 MPa, Λ_h cannot be distinguished from λ_h. In other words, these observations suggest that it is not necessarily correct to assume that the static moduli are always less than their equivalent dynamic moduli, at least for these anisotropic rocks.

Implications for geomechanical investigations

It is important to briefly explore the implications of these laboratory observations.

There are many consequences to the interpretation and use of sonic log data particularly with application to fluid detection and geomechanics by determining Poisson's ratio ν from the observed V_P/V_S ratio according to the well-known expression

$$\nu = \frac{1}{2}\frac{(V_P/V_S)^2 - 2}{(V_P/V_S)^2 - 1}. \tag{18}$$

Ignore for the moment the possibility of stress-induced anisotropy around the borehole and consider a vertical borehole drilled parallel to the x_3-axis of symmetry of the formation it passes through. Regardless of whether the sonic tool uses a monopole or dipole source, the shear waves propagating parallel to the borehole axis should be horizontally polarized and the wave speed measured akin to $V_{S(0)}$. Similarly, the tool would be expected to provide $V_{P(0)}$. For the sake of comparison, the "isotropic" ν calculated using these two wave speeds are also provided by red open circles in Figure 12d–12f. It does not appear that this ν is related in any systematic way to the anisotropic Poisson's ratios at least within this admittedly limited sample set.

This will have implications for the popular practice of using ν to predict the horizontal principal stress S_h or, alternatively, the fracture closure pressure using the vertical principal stress S_V via the assumption that the horizontal principal stress S_h is essentially

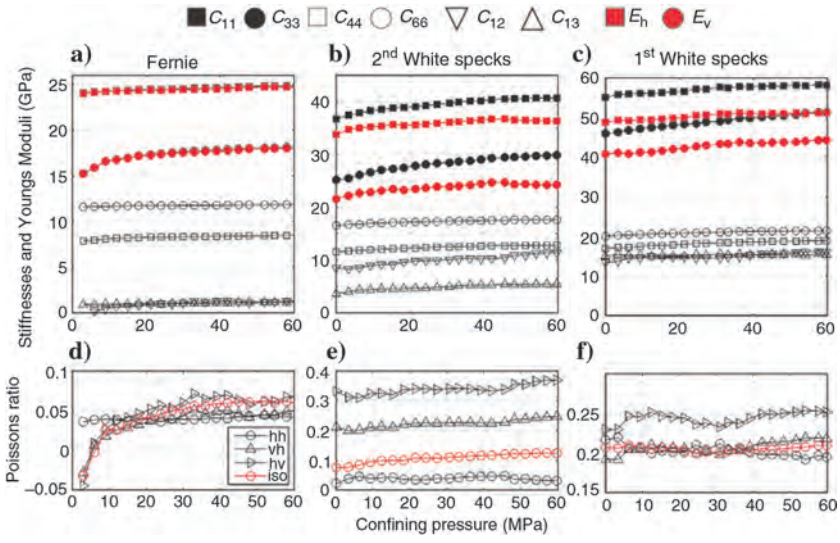

Figure 12. Calculated dynamic elastic stiffnesses and Young's moduli for (a) Fernie Formation sample SSA-24, (b) Second White Specks Formation sample SSA-27, and (c) First White Specks Formation sample SSA-42. Calculated dynamic Poisson's ratios according to ν_{hh} (open circles), ν_{vh} (open upward triangles), ν_{hv} (open right-pointing triangle), and isotropic ν calculated using equation 18 (open red circle) for (d) Fernie Formation sample SSA-24, (e) Second White Specks Formation sample SSA-27, and (f) First White Specks Formation sample SSA-42.

generated by horizontal confinement resistance to Poisson ratio expansion of a column of rock loaded gravitationally by the vertical principal stress S_V (Eaton, 1969; Thiercelin and Plumb, 1994)

$$S_h = \frac{\nu}{1-\nu} S_V. \tag{19}$$

It is not clear in which application of equation 19 originated, but it appears to have some roots in Hubbert and Willis' (1957) classic paper in which they suggest, in regions subject to normal faulting, that $S_h/S_V \sim 1/3$, which is the case for $\nu \sim 0.25$.

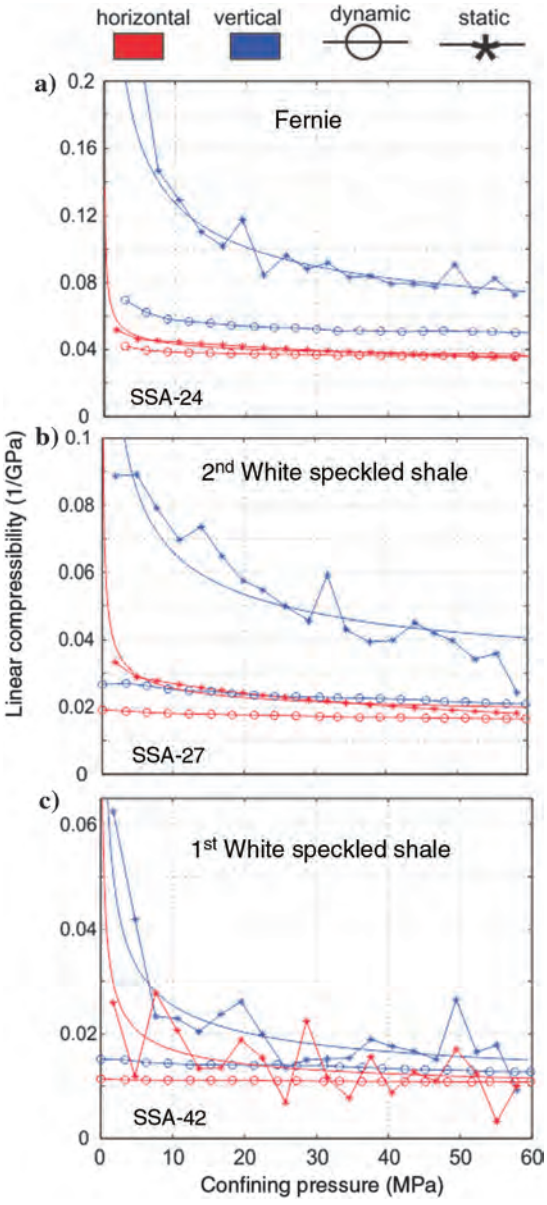

Figure 13. Comparison of static and dynamic moduli. Linear compressibilities for the horizontal (red) and bedding-perpendicular vertical (blue) directions obtained directly by taking slopes using simple differences (*) or nonlinear curve fitting (equation 17) to the observed $\varepsilon_{(90)}$ and $\varepsilon_{(0)}$ strain versus pressures curves of Figure 11 compared to their corresponding dynamic linear compressibilities (open circles) calculated using equation 14.

The uncertainty on value of ν obtained from the $V_{P(0)}/V_{S(0)}$ ratio makes applying equation 19 to estimate stress even more questionable. Under the same lateral constraint assumption, the horizontal stress induced by application of S_V to a TI formation is

$$S_h = \frac{\nu_{hv}}{1-\nu_{hh}} S_V. \tag{20}$$

The ratios between the horizontal stresses predicted by the isotropic assumption of equation 19 with the TI assumption of equation 20 are plotted for the four samples measured with confining pressure (Figure 14). Aside from a few excursions for sample SSA-24, this ratio is for the most part less than unity. The First White Speckled Shale sample SSA-42 is nearly isotropic, but for it, the predicted isotropic horizontal stress ranges from approximately 82% to 90% that of the anisotropic case. The ratio for the highly anisotropic Fernie Formation SSA-24 is close to unity, but there is a significant difference for the two Second White Speckled Shale samples SSA-27 and SSA-41 with the ratio from Figure 14 only 10% to 40%. This large deviation stems primarily from the significant magnitude the off-axis C_{12} and C_{13} terms of which are responsible for coupling the vertical to the horizontal loads. In summary, examination of Figure 14 further demonstrates the large uncertainties associated with attempts to quantitatively determine horizontal stress magnitudes using equations 19 and 20.

Another important, and perhaps somewhat unexpected, result from the present measurements is the related observations that $\lambda_{(90)}$ and $V_{S(90)}$ are nearly constant over the range of confining pressures applied. In other words, the bedding-parallel elastic properties are largely insensitive to the stress. The heuristic physical interpretation of this is that there are not significant numbers of small aspect ratio cracklike pores with planes aligned perpendicular to the bedding, which is certainly consistent with the SEM images shown

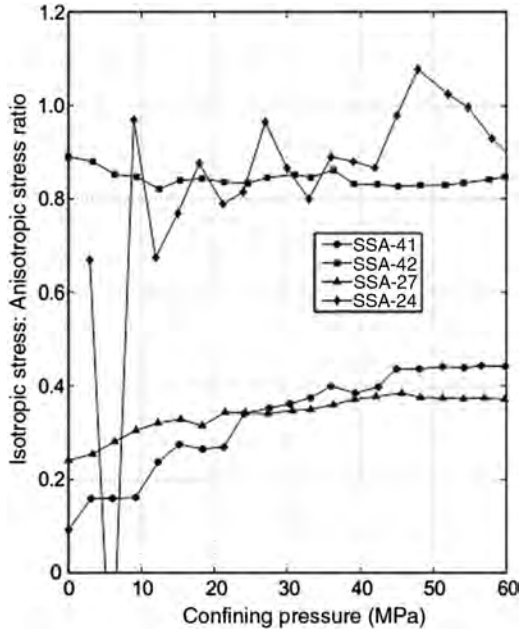

Figure 14. Ratio between the horizontal stresses estimated under the lateral constraint assumption between the isotropic model that uses only ν obtained from vertical propagating P- and S-wave speeds and the TI model that incorporates anisotropic Poisson's ratios.

above and with the modeling results reported by Sarout and Guéguen (2008b).

Consider again a borehole drilled perpendicular to the bedding planes. It is well-known that the circular borehole cavity predictably concentrates the tectonic stresses. However, rock is generally nonlinearly elastic and deviatoric stresses result in azimuthal variations in the moduli around the borehole (see Schmitt et al., 2012). The variations in moduli can be substantial; for example, Winkler (1996) observes azimuthal variations in upward of 17% around a borehole drilled into a block of Berea sandstone subject to an uniaxial stress of only 10 MPa. However, in samples SSA-24 and SSA-27, any azimuthal variations in the moduli may be largely absent. The uniformity of the moduli around the borehole will have implications for the interpretation of crossed-dipole sonic logs for stress directions. Such logging tools include two orthogonal sets of dipole sources (Tang and Cheng, 2004). Upon activation, these sources set up flexural wave modes along the borehole with polarizations aligned with the azimuthal variations in the moduli around the borehole regardless of whether they exist because of the intrinsic material anisotropy or they are induced by stress concentrations (e.g., Plona et al., 2002). If azimuthal variations are not present, then the polarization of the flexural waves cannot indicate stress directions.

CONCLUSIONS

We measured the elastic anisotropy on four representative shales, two of which are highly prospective as unconventional hydrocarbon resources. Ultrasonic measurements allowed for the determination of the complete set of dynamic TI stiffnesses whereas simultaneous strain measurements gave static linear compressibilities. The pressure sensitivity of the strains and the wave speeds differed depending on the direction. The waves speeds and strain perpendicular to the bedding plane (here assumed to be the plane of isotropy under the presumption that the rocks are TI) are nonlinearly dependent on the confining pressure. In contrast, the speeds and strains along the bedding plane vary linearly suggesting that there is little vertically oriented compliant microcrack porosity. Consequently, the elastic stiffnesses C_{11} and C_{66} are not significantly influenced by stress; this lack of stress sensitivity may have implications for the interpretation of certain types of sonic logs for stress directions.

Comparison of dynamic to static moduli has long been a concern, and it is usually assumed that the latter is always a substantial fraction of the former. We found this to be true for those measurements made perpendicular to the bedding plane, but unexpectedly the static and dynamic moduli within the bedding plane are nearly equal. Given that the bedding-perpendicular and bedding-parallel planes display quite different pressure sensitivities, it is likely that the degree of deviation between the static and dynamic moduli depends strongly on the existence of compliant cracklike porosity. To our knowledge, no rigorous solution to this problem has been found and workers usually just ascribe it to "dispersion." However, further theoretical investigations of this issue may indeed assist in explaining the dispersion of seismic wave propagation that we do see.

The anisotropic moduli determined here were also used to test the validity of the now widely applied practice of estimating "fracture gradient pressures" using sonic-log-derived Poisson's ratios. We found that the horizontal stresses estimated in ignorance of the anisotropy could not in any systematic way be related to those estimated using the full set of TI moduli. We hope that these results will further discourage this practice and encourage operators to use more rigorous methods such as mutlicycle hydraulic fracturing tests to quantitatively estimate horizontal stress magnitudes.

Finally, this work provides yet some additional values for sedimentary rock anisotropy. The paper has primarily focused on applications to geomechanics, but it still is important in applied seismologic studies. Two of the shales studied here have relatively high ε and γ approaching 0.2. In contrast, prestack anisotropic depth migration of seismic data in the disturbed belt of western Alberta typically uses values of $\varepsilon < 0.1$. Examination of further core samples may help to refine the values of ε that should be used.

The sophistication of in the descriptions of rock properties that geophysicists have used has evolved rapidly with the strong interest in anisotropy over the last quarter century and with growing attention to stress-dependent nonlinearity effects. The results here demonstrate that we may need to examine combinations of these two aspects as the present measurements clearly show anisotropy in the nonlinear behavior.

ACKNOWLEDGMENTS

J. Meléndez-Martínez was supported by a scholarship from the Mexican Petroleum Institute. D. R. Schmitt was supported by the Canada Research Chairs program. C. D. Rokosh assisted in the collection of the core samples. The laboratory measurements were greatly assisted by R. Kofman, L. Tober, and L. Duerksen. O. N. Ong assisted with TOC determinations.

REFERENCES

Abell, B. C., and L. J. Pyrak-Nolte, 2013, Coupled wedge waves: Journal of the Acoustical Society of America, **134**, 3551–3560, doi: 10.1121/1.4821987.

Abell, B. C., S. Y. Shao, and L. J. Pyrak-Nolte, 2014, Measurements of elastic constants in anisotropic media: Geophysics, **79**, no. 5, D349–D362, doi: 10.1190/geo2014-0023.1.

Allan, A. M., W. Kanitpanyacharoen, and T. Vanorio, 2015, A multiscale methodology for the analysis of velocity anisotropy in organic-rich shale: Geophysics, **80**, no. 4, C73–C88, doi: 10.1190/geo2014-0192.1.

Amadei, B., 1983, Rock anisotropy and the theory of stress measurements: Springer-Verlag.

Arroyo, M., and D. Muir Wood, 2003, Simplifications related to dynamic measurements of anisotropic G(0): International Symposium on Deformation Behaviour of Geomaterials, 1233–1239.

Auld, B. A., 1973, Acoustic fields and waves in solids: Wiley-Interscience Publication.

Bakhorji, A. M., 2010, Laboratory measurements of static and dynamic elastic properties in carbonate: Ph.D. thesis, University of Alberta.

Banik, N. C., 1984, Velocity anisotropy of shales and depth estimation in the North-Sea Basin: Geophysics, **49**, 1411–1419, doi: 10.1190/1.1441770.

Behura, J., M. Batzle, R. Hofmann, and J. Dorgan, 2009, Oil shales: Their shear story: The Leading Edge, **28**, 850–855, doi: 10.1190/1.3167788.

Biot, M. A., 1956a, Theory of propagation of elastic waves in a fluid-saturated porous solid. 1. Low-frequency range: Journal of the Acoustical Society of America, **28**, 168–178, doi: 10.1121/1.1908239.

Biot, M. A., 1956b, Theory of propagation of elastic waves in a fluid-saturated porous solid. 2. Higher frequency range: Journal of the Acoustical Society of America, **28**, 179–191, doi: 10.1121/1.1908241.

Bloch, J., C. Schröder-Adams, D. Leckie, J. Craig, and D. McIntyre, 1999, Sedimentology, micropaleontology, geochemistry, and hydrocarbon potential of shale from the Cretaceous Lower Colorado Group in western Canada: Geological Survey of Canada Bulletin 531, Geological Survey of Canada.

Blum, T. E., L. Adam, and K. van Wijk, 2013, Noncontacting benchtop measurements of the elastic properties of shales: Geophysics, **78**, no. 3, C25–C31, doi: 10.1190/geo2012-0314.1.

Bouzidi, Y., and D. R. Schmitt, 2006, A large ultrasonic bounded acoustic pulse transducer for acoustic transmission goniometry: Modeling and calibration: Journal of the Acoustical Society of America, **119**, 54–64, doi: 10.1121/1.2133683.

Bower, A. F., 2010, Applied mechanics of solids (1st ed.): CRC Press.

Brace, W. F., 1964, Effect of pressure on electric-resistance strain gages: Experimental Mechanics, **4**, 212–216, doi: 10.1007/BF02323653.
Brace, W. F., 1965, Some new measurements of linear compressibility of rocks: Journal of Geophysical Research, **70**, 391–398, doi: 10.1029/JZ070i002p00391.
Carcione, J. M., 2007, Wave fields in real media: Wave propagation in anisotropic, anelastic, porous and electromagnetic media: Handbook of Geophysical Exploration (2nd ed.): Elsevier Science.
Chan, J., and D. R. Schmitt, 2015, Elastic anisotropy of a metamorphic rock sample of the Canadian Shield in Northeastern Alberta: Rock Mechanics and Rock Engineering, **48**, 1369–1385, doi: 10.1007/s00603-014-0664-z.
Cheadle, S. P., R. J. Brown, and D. C. Lawton, 1991, Orthorhombic anisotropy — A physical seismic modeling study: Geophysics, **56**, 1603–1613, doi: 10.1190/1.1442971.
Chenevert, M. E., and C. Gatlin, 1965, Mechanical anisotropies of laminated sedimentary rocks: SPE Journal, **5**, 67–77, doi: 10.2118/890-PA.
Cheng, C. H., and D. H. Johnston, 1981, Dynamic and static moduli: Geophysical Research Letters, **8**, 39–42, doi: 10.1029/GL008i001p00039.
Cheng, Q., C. Sondergeld, and C. Rai, 2013, Experimental study of rock strength anisotropy and elastic modulus anisotropy: 83rd Annual International Meeting, SEG, Expanded Abstracts, 362–367.
Cholach, P. Y., and D. R. Schmitt, 2006, Intrinsic elasticity of a textured transversely isotropic muscovite aggregate: Comparisons to the seismic anisotropy of schists and shales: Journal of Geophysical Research: Solid Earth, **111**, doi: 10.1029/2005JB004158.
Curtis, J. B., 2002, Fractured shale-gas systems: AAPG Bulletin, **86**, 1921–1938.
Dean, W. E., 2007, Sediment geochemical records of productivity and oxygen depletion along the margin of western North America during the past 60,000 years: Teleconnections with Greenland Ice and the Cariaco Basin: Quaternary Science Reviews, **26**, 98–114, doi: 10.1016/j.quascirev.2006.08.006.
Dellinger, J., and L. Vernik, 1994, Do travel-times in pulse-transmission experiments yield anisotropic group or phase velocities?: Geophysics, **59**, 1774–1779, doi: 10.1190/1.1443564.
Dewhurst, D. N., and A. F. Siggins, 2006, Impact of fabric, microcracks and stress field on shale anisotropy: Geophysical Journal International, **165**, 135–148, doi: 10.1111/j.1365-246X.2006.02834.x.
Dewhurst, D. N., A. F. Siggins, J. Sarout, M. D. Raven, and H. M. Nordgard-Bolas, 2011, Geomechanical and ultrasonic characterization of a Norwegian Sea shale: Geophysics, **76**, no. 3, WA101–WA111, doi: 10.1190/1.3569599.
Douglas, C. C., G. Qin, N. Collier, and B. Gong, 2011, Intelligent fracture creation for shale gas development: Proceedings of the International Conference on Computational Science, Procedia Computer Science, **4**, 1745–1750.
Eaton, B. A., 1969, Fracture gradient prediction and its application in oilfield operations: Journal of Petroleum Technology, **21**, 1353–1360, doi: 10.2118/2163-PA.
Every, A. G., and W. Sachse, 1990, Determination of the elastic-constants of anisotropic solids from acoustic-wave group-velocity measurements: Physical Review B, **42**, 8196–8205, doi: 10.1103/PhysRevB.42.8196.
Furmann, A., M. Mastalerz, S. C. Brassell, P. K. Pedersen, N. A. Zajac, and A. Schimmelmann, 2015, Organic matter geochemistry and petrography of Late Cretaceous (Cenomanian-Turonian) organic-rich shales from the Belle Fourche and Second White Specks formations, west-central Alberta, Canada: Organic Geochemistry, **85**, 102–120, doi: 10.1016/j.orggeochem.2015.05.002.
Gardner, G. H. F., M. R. J. Wyllie, and D. M. Droschak, 1965, Hysteresis in the velocity-pressure characteristics of rocks: Geophysics, **30**, 111–116, doi: 10.1190/1.1439524.
Gassmann, F., 1951, Über die Elastizität poröser Medien: Kümmerly & Frey.
Gautam, R., and R. C. K. Wong, 2006, Transversely isotropic stiffness parameters and their measurement in Colorado shale: Canadian Geotechnical Journal, **43**, 1290–1305, doi: 10.1139/t06-083.
Giesche, H., 2006, Mercury porosimetry: A general (practical) overview: Particle and Particle Systems Characterization, **23**, 9–19, doi: 10.1002/ppsc.200601009.
Hemsing, D. B., 2007, Laboratory determination of seismic anisotropy in sedimentary rock from the Western Canadian Sedimentary Basin: M.S. thesis, University of Alberta.
Higgins, S. M., S. A. Goodwin, A. Donald, T. R. Bratton, and G. W. Tracy, 2008, Anisotropic stress models improve completion design in the Baxter Shale: Annual Technical Conference and Exhibition, SPE-115736.
Holt, R. M., O. M. Nes, J. F. Stenebraten, and E. Fjaer, 2012, Static versus dynamic behavior of shale: 46th U.S. Rock Mechanics/Geomechanics Symposium, ARMA 2012-542.
Hornby, B. E., 1998, Experimental laboratory determination of the dynamic elastic properties of wet, drained shales: Journal of Geophysical Research: Solid Earth, **103**, 29945–29964, doi: 10.1029/97JB02380.
Horsrud, P., E. F. Sonstebo, and R. Boe, 1998, Mechanical and petrophysical properties of North Sea shales: International Journal of Rock Mechanics and Mining Sciences, **35**, 1009–1020, doi: 10.1016/S0148-9062(98)00162-4.
Hubbert, M., and D. Willis, 1957, Mechanics of hydraulic fracturing: AIME Petroleum Transactions, **210**, 153–163.
Iverson, W. P., 1995, Closure stress calculations in anisotropic formations: Low Permeability Reservoirs Symposium, SPE 29598-MS.
Jakobsen, M., and T. A. Johansen, 2000, Anisotropic approximations for mudrocks: A seismic laboratory study: Geophysics, **65**, 1711–1725, doi: 10.1190/1.1444856.
Johnston, J. E., and N. I. Christensen, 1994, Elastic-constants and velocity surfaces of indurated anisotropic shales: Surveys in Geophysics, **15**, 481–494, doi: 10.1007/BF00690171.
Jones, L. E. A., and H. F. Wang, 1981, Ultrasonic velocities in cretaceous shales from the Williston Basin: Geophysics, **46**, 288–297, doi: 10.1190/1.1441199.
Kaarsberg, E. A., 1959, Introductory studies of natural and artificial argillaceous aggregates by sound-propagation and x-ray diffraction methods: Journal of Geology, **67**, 447–472, doi: 10.1086/626597.
Kalani, M., J. Jahren, N. H. Mondol, and J. I. Faleide, 2015, Petrophysical implications of source rock microfracturing: International Journal of Coal Geology, **143**, 43–67, doi: 10.1016/j.coal.2015.03.009.
Kebaili, A., and D. R. Schmitt, 1997, Ultrasonic anisotropic phase velocity determination with the Radon transformation: Journal of the Acoustical Society of America, **101**, 3278–3286, doi: 10.1121/1.418344.
King, M. S., 1983, Static and dynamic elastic properties of rocks from the Canadian Shield: International Journal of Rock Mechanics and Mining Sciences, **20**, 237–241, doi: 10.1016/0148-9062(83)90004-9.
King, M. S., M. Andrea, and M. Shams Khanshir, 1994, Velocity anisotropy of carboniferous mudstones: International Journal of Rock Mechanics and Mining Sciences and Geomechanics Abstracts, **31**, 261–263, doi: 10.1016/0148-9062(94)90470-7.
Kloubek, J., 1981, Hysteresis in porosimetry: Powder Technology, **29**, 63–73, doi: 10.1016/0032-5910(81)85005-X.
Kular, G., 1972, Use of foil strain gage at high hydrostatic pressure: Experimental Mechanics, **12**, 311–316, doi: 10.1007/BF02320486.
Leckie, D., J. Bhattacharya, J. Bloch, C. Gilboy, and B. Norris, 1994, Cretaceous Colorado/Alberta Group of the Western Canada Sedimentary Basin, *in* G. D. Mossop, and I. Shetsen, eds., Geological Atlas of the Western Canada Sedimentary Basin: Canadian Society of Petroleum Geologists and Alberta Research Council, chapter 20, 335–352.
Lekhnitskii, S., 1981, Theory of elasticity of an anisotropic body: Mir Publications.
Lempriere, B. M., 1968, Poisson's ratio in orthotropic materials: AIAA Journal, **6**, 2226–2227, doi: 10.2514/3.4974.
Lethbridge, Z. A. D., R. I. Walton, A. S. H. Marmier, C. W. Smith, and K. E. Evans, 2010, Elastic anisotropy and extreme Poisson's ratios in single crystals: Acta Materialia, **58**, 6444–6451, doi: 10.1016/j.actamat.2010.08.006.
Li, Y., 1976, The anisotropic behavior of Poisson's ratio, Young's modulus, and shear modulus in hexagonal materials: Physica Status Solidi A: Applied Research, **38**, 171–175, doi: 10.1002/pssa.2210380119.
Liao, J. J., T.-B. Hu, and C.-W. Chang, 1997, Determination of dynamic elastic constants of transversely isotropic rocks using a single cylindrical specimen: International Journal of Rock Mechanics and Mining Sciences, **34**, 1045–1054, doi: 10.1016/S1365-1609(97)90198-2.
Lings, M. L., 2001, Drained and undrained anisotropic elastic stiffness parameters: Geotechnique, **51**, 555–565, doi: 10.1680/geot.2001.51.6.555.
Lokajicek, T., and T. Svitek, 2015, Laboratory measurement of elastic anisotropy on spherical rock samples by longitudinal and transverse sounding under confining pressure: Ultrasonics, **56**, 294–302, doi: 10.1016/j.ultras.2014.08.015.
Love, A. E. H., 1892, A treatise on the mathematical theory of elasticity: Cambridge University Press.
Lubarda, V. A., and M. C. Chen, 2008, On the elastic moduli and compliances of transversely isotropic and orthotropic materials: Journal of Mechanics of Materials and Structures, **3**, 153–171, doi: 10.2140/jomms.2008.3.153.
Mah, M., and D. R. Schmitt, 2001, Experimental determination of the elastic coefficients of an orthorhombic material: Geophysics, **66**, 1217–1225, doi: 10.1190/1.1487068.
Mah, M., and D. R. Schmitt, 2003, Determination of the complete elastic stiffnesses from ultrasonic phase velocity measurements: Journal of Geophysical Research: Solid Earth, **108**, ECV 6-1–ECV 6-11, doi: 10.1029/2001JB001586.
Mahmoudian, F., G. F. Margrave, P. F. Daley, J. Wong, and D. C. Henley, 2014, Estimation of elastic stiffness coefficients of an orthorhombic physical model using group velocity analysis on transmission data: Geophysics, **79**, no. 1, R27–R39, doi: 10.1190/geo2013-0203.1.
Marmier, A., Z. A. D. Lethbridge, R. I. Walton, C. W. Smith, S. C. Parker, and K. E. Evans, 2010, ElAM: A computer program for the analysis and

representation of anisotropic elastic properties: Computer Physics Communications, **181**, 2102–2115, doi: 10.1016/j.cpc.2010.08.033.
Mavko, G., and A. Nur, 1975, Melt squirt in asthenosphere: Journal of Geophysical Research, **80**, 1444–1448, doi: 10.1029/JB080i011p01444.
McLamore, R., and K. E. Gray, 1967, The mechanical behavior of anisotropic sedimentary rocks: Journal of Manufacturing Science and Engineering, **89**, 62–73, doi: 10.1115/1.3610013.
Meléndez-Martínez, J., 2014, Elastic properties of sedimentary rocks: Ph.D. thesis, University of Alberta.
Meléndez-Martínez, J., and D. R. Schmitt, 2013, Anisotropic elastic moduli of carbonates and evaporites from the Weyburn-Midale reservoir and seal rocks: Geophysical Prospecting, **61**, 363–379, doi: 10.1111/1365-2478.12032.
Meyer, B. R., and R. H. Jacot, 2001, Impact of stress-dependent Young's moduli on hydraulic fracture modeling, *in* D. Elsworth, J. P. Tinucci, and K. A. Heasley, eds., Rock Mechanics in the National Interest, vol. **1**: CRC Press.
Meyer, P., 2012, Shale source rocks a game-changer due to 8-to-1 resource potential: Oil and Gas Journal, **110**, 72–74.
Milligan, R. V., 1967, The gross hydrostatic-pressure effect as related to foil and wire strain gages: Experimental Mechanics, **7**, 67–74, doi: 10.1007/BF02326709.
Molyneux, J. B., and D. R. Schmitt, 2000, Compressional-wave velocities in attenuating media: A laboratory physical model study: Geophysics, **65**, 1162–1167, doi: 10.1190/1.1444809.
Nadri, D., J. Sarout, A. Bóna, and D. Dewhurst, 2012, Estimation of the anisotropy parameters of transversely isotropic shales with a tilted symmetry axis: Geophysical Journal International, **190**, 1197–1203, doi: 10.1111/j.1365-246X.2012.05545.x.
Nara, Y., H. Kato, T. Yoneda, and K. Kaneko, 2011, Determination of three-dimensional microcrack distribution and principal axes for granite using a polyhedral specimen: International Journal of Rock Mechanics and Mining Sciences, **48**, 316–335, doi: 10.1016/j.ijrmms.2010.08.009.
Nemeth, M. P., 2011, An in-depth tutorial on constitutive equations for elastic anisotropic materials: NASA Technical Memorandum, NASA Center for AeroSpace Information.
Niandou, H., J. F. Shao, J. P. Henry, and D. Fourmaintraux, 1997, Laboratory investigation of the behaviour of Tournemire shale: International Journal of Rock Mechanics and Mining Sciences, **34**, 3–16, doi: 10.1016/S1365-1609(97)80029-9.
Nielsen, K. S., C. J. Schröder-Adams, and D. A. Leckie, 2003, A new stratigraphic framework for the Upper Colorado Group (Cretaceous) in southern Alberta and southwestern Saskatchewan, Canada: Bulletin of Canadian Petroleum Geology, **51**, 304–346, doi: 10.2113/51.3.304.
Nye, J. F., 1985, Physical properties of crystals: Oxford University Press.
Ohno, I., M. Abe, M. Kimura, Y. Hanayama, H. Oda, and I. Suzuki, 2000, Elasticity measurement of silica glass under gas pressure: American Mineralogist, **85**, 288–291, doi: 10.2138/am-2000-2-304.
Pawlowicz, J. G., S. D. A. Anderson, C. D. Rokosh, and A. P. Beaton, 2008, Mineralogy, permeametry, mercury porosimetry and scanning electron microscope imaging of the Colorado Group: Shale gas data release: Alberta Geological Survey Open File Report 2008-14, Energy Resources Conservation Board.
Pickering, D. J., 1970, Anisotropic elastic parameters for soil: Geotechnique, **20**, 271–276, doi: 10.1680/geot.1970.20.3.271.
Plona, T. J., M. R. Kane, B. Sinha, and J. Walsh, 2002, Evaluating stress-induced anisotropy and mechanical damage from cross-dipole sonic data using dispersion analysis: Rock Mechanics Conference, SPE/ISRM 78233.
Raymond, G. P., 1970, Stresses and displacements in cross-anisotropic soil: Geotechnique, **20**, 456–458, doi: 10.1680/geot.1970.20.4.456.
Rokosh, C. D., S. Lyster, S. D. A. Anderson, A. P. Beaton, H. Berhane, T. Brazzoni, D. Chen, Y. Cheng, T. Mack, C. Pana, and J. G. Pawlowicz, 2012, Summary of Alberta's shale and siltstone-hosted hydrocarbons, http://ags.aer.ca/document/OFR/OFR_2012_06.PDF, accessed 07 March 2016.
Rovati, M., 2003, On the negative Poisson's ratio of an orthorhombic alloy: Scripta Materialia, **48**, 235–240, doi: 10.1016/S1359-6462(02)00386-X.
Sarout, J., L. Esteban, C. Delle Piane, B. Maney, and D. N. Dewhurst, 2014, Elastic anisotropy of Opalinus Clay under variable saturation and triaxial stress: Geophysical Journal International, **198**, 1662–1682, doi: 10.1093/gji/ggu231.
Sarout, J., and Y. Guéguen, 2008a, Anisotropy of elastic wave velocities in deformed shales: Part 1 — Experimental results: Geophysics, **73**, no. 5, D75–D89, doi: 10.1190/1.2952744.
Sarout, J., and Y. Guéguen, 2008b, Anisotropy of elastic wave velocities in deformed shales: Part 2 — Modeling results: Geophysics, **73**, no. 5, D91–D103, doi: 10.1190/1.2952745.
Sarout, J., L. Molez, Y. Guéguen, and N. Hoteit, 2007, Shale dynamic properties and anisotropy under triaxial loading: Experimental and theoretical investigations: Physics and Chemistry of the Earth, **32**, 896–906, doi: 10.1016/j.pce.2006.01.007.
Sayers, C. M., 2004, Seismic anisotropy of shales: What determines the sign of Thomsen's delta parameter?: 74th Annual International Meeting, SEG, Expanded Abstracts, 103–106.
Sayers, C. M., 2013, The effect of anisotropy on the Young's moduli and Poisson's ratios of shales: Geophysical Prospecting, **61**, 416–426, doi: 10.1111/j.1365-2478.2012.01130.x.
Schmitt, D. R., 2015, Geophysical properties of the near surface earth: Seismic properties, *in* G. Schubert, ed., Treatise on geophysics (2nd ed.): Elsevier 11, 43–87.
Schmitt, D. R., C. A. Currie, and L. Zhang, 2012, Crustal stress determination from boreholes and rock cores: Fundamental principles: Tectonophysics, **580**, 1–26, doi: 10.1016/j.tecto.2012.08.029.
Simmons, G., and W. F. Brace, 1965, Comparison of static and dynamic measurements of compressibility of rocks: Journal of Geophysical Research, **70**, 5649–5656, doi: 10.1029/JZ070i022p05649.
Sondergeld, C. H., R. J. Ambrose, C. S. Rai, and J. Moncrieff, 2010, Microstructural studies of gas shales: Unconventional Gas Conference, SPE 131771.
Sondergeld, C. H., and C. S. Rai, 1992, Laboratory observations of shear-wave propagation in anisotropic media: The Leading Edge, **11**, 38–43, doi: 10.1190/1.1436871.
Sone, H., and M. D. Zoback, 2013, Mechanical properties of shale-gas reservoir rocks — Part 1: Static and dynamic elastic properties and anisotropy: Geophysics, **78**, no. 5, D378–D389, doi: 10.1190/geo2013-0050.1.
Spikes, K. T., 2014, Error estimates of elastic components in stress-dependent VTI media: Journal of Applied Geophysics, **108**, 110–123, doi: 10.1016/j.jappgeo.2014.06.015.
Tang, X. M., and A. Cheng, 2004, Quantitative borehole acoustic methods: Elsevier.
Thiercelin, M. J., and R. A. Plumb, 1994, A core-based prediction of lithologic stress contrasts in east Texas formations: SPE Formation Evaluation, **9**, 251–258, doi: 10.2118/21847-PA.
Thomsen, L., 1986, Weak elastic anisotropy: Geophysics, **51**, 1954–1966, doi: 10.1190/1.1442051.
Ting, T. C. T., 2004, Very large Poisson's ratio with a bounded transverse strain in anisotropic elastic materials: Journal of Elasticity, **77**, 163–176, doi: 10.1007/s10659-005-2156-6.
Ting, T. C. T., and T. Y. Chen, 2005, Poisson's ratio for anisotropic elastic materials can have no bounds: Quarterly Journal of Mechanics and Applied Mathematics, **58**, 73–82, doi: 10.1093/qjmamj/hbh021.
Tutuncu, A. N., A. L. Podio, A. R. Gregory, and M. M. Sharma, 1998, Nonlinear viscoelastic behavior of sedimentary rocks, Part I: Effect of frequency and strain amplitude: Geophysics, **63**, 184–194, doi: 10.1190/1.1444311.
Vernik, L., and X. Z. Liu, 1997, Velocity anisotropy in shales: A petrophysical study: Geophysics, **62**, 521–532, doi: 10.1190/1.1444162.
Vernik, L., and A. Nur, 1992, Ultrasonic velocity and anisotropy of hydrocarbon source rocks: Geophysics, **57**, 727–735, doi: 10.1190/1.1443286.
Wang, H. F., 2000, The linear theory of poroelasticity with applications to geomechanics and hydrology: Princeton University Press.
Wang, Z. J., 2002, Seismic anisotropy in sedimentary rocks, Part 2: Laboratory data: Geophysics, **67**, 1423–1440, doi: 10.1190/1.1512743.
Wardlaw, N. C., and M. McKellar, 1981, Mercury porosimetry and the interpretation of pore geometry in sedimentary-rocks and artificial models: Powder Technology, **29**, 127–143, doi: 10.1016/0032-5910(81)85011-5.
Winkler, K. W., 1996, Azimuthal velocity variations caused by borehole stress concentrations: Journal of Geophysical Research: Solid Earth, **101**, 8615–8621, doi: 10.1029/96JB00093.
Wong, R. C. K., D. R. Schmitt, D. Collis, and R. Gautam, 2008, Inherent transversely isotropic elastic parameters of over-consolidated shale measured by ultrasonic waves and their comparison with static and acoustic in situ log measurements: Journal of Geophysics and Engineering, **5**, 103–117, doi: 10.1088/1742-2132/5/1/011.
Wright, J., 1987, The effects of transverse isotropy on reflection amplitude versus offset: Geophysics, **52**, 564–567, doi: 10.1190/1.1442325.
Xie, J., B. Di, J. Wei, X. Luan, and P. Ding, 2015, Feasibility of theoretical formulas on the anisotropy of shale based on laboratory measurement and error analysis: Journal of Geophysics and Engineering, **12**, 253–261, doi: 10.1088/1742-2132/12/2/253.
Zhang, J. C., 2013, Borehole stability analysis accounting for anisotropies in drilling to weak bedding planes: International Journal of Rock Mechanics and Mining Sciences, **60**, 160–170, doi: 10.1016/j.ijrmms.2012.12.025.